Efficient 3D modelling of punching shear failure at slab-column connections by means of nonlinear joint elements

Andri Setiawan
PhD candidate, Department of Civil and Environmental Engineering, Imperial College London, London, United Kingdom

Robert L Vollum
Reader in Concrete Structures, Department of Civil and Environmental Engineering, Imperial College London, London, United Kingdom

Lorenzo Macorini
Senior Lecturer in Structural Engineering, Department of Civil and Environmental Engineering, Imperial College London, London, United Kingdom

Bassam Izzuddin
Professor of Computational Structural Mechanics, Department of Civil and Environmental Engineering, Imperial College London, London, United Kingdom

Notation

a_t	slope of concrete tension softening curve
b_0	length of control perimeter (with rounded corners) at a distance of the half of the average flexural effective depth from the column face
$b_{0,3d}$	effective (reduced) control perimeter length by limiting the longer side to *3d*
b_c	factor for biaxial compressive interaction
c_{max}	longer dimension of a rectangular column
c_{min}	shorter dimension of a rectangular column
d	average flexural effective depth of the slab
d_g	maximum aggregate size
d_{g0}	reference aggregate size equal to 16 mm
d_{dg}	parameter representing the crack average roughness
Δd_i	relative displacement at joint nodes at current step (i)
e	eccentricity of the resultant shear force with respect to the centroid of the basic control perimeter
E_c	concrete elastic modulus
$f_{c'}$	concrete compressive strength
f_t	concrete tensile strength
GSR	ratio of applied gravity force to the punching capacity of a reference slab tested under concentric loading
k	empirical coefficient to calculate nominal one-way shear resistance
k_{deg}	descending stiffness of joint element
k_i	joint tangent stiffness at current step (i)
k_{inc}	initial ascending stiffness of joint element
k_{red}	stiffness reduction factor for joint elements
l_s	spacing between adjacent joint elements
L	slab span between column centrelines
n	number of joint elements around full control perimeter
n_{nef}	number of joint elements outside the effective control perimeter for punching
P_{test}	measured failure load from experimental test
P_u	predicted failure load
r_c	normalised residual compressive strength
s_c	normalised initial compressive strength
t	slab thickness

v	concrete Poisson's ratio
v_c	nominal one-way shear resistance per unit length
v_{c_min}	minimum one-way shear resistance per unit length
V_{1_way}	one-way shear capacity assigned to joint elements outside effective control perimeter
V_{cap}	shear resistance of individual joint element
$V_{CSCT(\psi x\text{-}\psi y)}$	modified punching load capacity for non-axis-symmetrical condition
V_i	joint shear force at current step (i)
V_{i-1}	joint shear force at previous step (i-1)
V_{pp}	post-punching resistance of joint element
V_R	punching load capacity
β	ratio of maximum to average shear stress along the control perimeter
β_s	shear retention factor for shell elements
δ	vertical joint separation to calculate notional spring length
γ	equivalent shear strain to calculate notional spring length
γ_s	normalised shear softening relative to direct tensile softening
ε_{ft0}	strain at which softening branch of concrete tensile stress reduces to zero
ε_s	strain at longitudinal reinforcement bars
ε_{sy}	yield strain of reinforcement bars
ε_{xc}, ε_{yc}	concrete crack strains
ρ_{top}	top flexural reinforcement ratio
ρ_x	top flexural reinforcement ratio parallel to x-axis
ρ_y	top flexural reinforcement ratio parallel to y-axis
σ_n	compressive membrane stress
σ_{xt}, σ_{yt}, τ_{xyt}	biaxial stresses in concrete
ϕ_s	factor scaling direct tensile stresses for shear interaction
ψ	slab rotation
ψ_s	slab rotation for individual sector element
ψ'	refined slab rotation under pre-stressing
ψ_{i-1}	monitored slab rotation at previous step (i-1)
ψ	

Abstract

Failures of isolated slab-column connections can be classified as either flexural or punching. Flexural failure is typically preceded by large deformation, owing to flexural reinforcement yield, unlike punching failure which occurs suddenly with little if any warning. This paper proposes a novel numerical strategy for modelling punching failure in which nonlinear joint elements are combined with nonlinear reinforced concrete (RC) shell elements. The joint elements are employed to model punching failure which limits force transfer from slabs to supporting columns. The shear resistance of individual joint element is calculated using the critical shear crack theory (CSCT) which relates shear resistance to slab rotation. Unlike other similar models reported in the literature, the joint strength is continually updated throughout the analysis as the slab rotation changes. The approach is presented for slabs without shear reinforcement but could be easily extended to include shear reinforcement. The adequacy of the proposed methodology is verified using experimental test data from isolated internal RC slab-column connections tested to failure under various loading arrangements and slab edge boundary conditions. Comparisons are also made with the predictions of nonlinear finite element analysis using 3-D solid elements, where the proposed methodology is shown to compare favourably

whilst requiring significantly less computation time. Additionally, the proposed methodology enables simple calculation of the relative contributions of flexure, torsion and eccentric shear to moment transfer between slab and column. This information is pertinent to the development of improved codified design methods for calculating the critical design shear stress at eccentrically loaded columns.

1 Introduction

Punching failure is still the subject of considerable research. Most codified design provisions for punching shear including ACI 318-14 [1] and EC2 [2] are empirically derived using data from tests on isolated slab-column connections which are unrepresentative of continuous flat slabs. The conservative nature of this approach is highlighted in a recent study by Einpaul et al. [3] which found that flexural continuity and compressive membrane action increase punching strength but reduce deformation capacity compared with conventional isolated test specimens.

Punching failure of flat slabs is more realistically simulated using 3-D solid elements capable of capturing the complex triaxial stress state around the column. This approach has the downside of being computationally expensive. Flexural behaviour is more efficiently modelled using classical nonlinear 2-D shell elements which need modification to model out-of-plane shear failure. Previous studies employing these two numerical approaches are briefly reviewed below along with their advantages and disadvantages.

Classical shell elements typically consider concrete nonlinearity only for in-plane biaxial stress with out-of-plane shear response modelled as linearly elastic. This enables realistic representation of flexural response but not punching failure. Attempts at modifying classical shell elements to capture punching failure can be classified into two main approaches. The first approach modifies the shell element formulation to account for transverse shear effects as done by Polak [4] who developed a layered-shell element, based on the modified compression field theory (MCFT) [5], for modelling the interaction between flexure and transverse shear. A constant transverse strain distribution is adopted through the thickness of the slab and the shear modulus is assumed to decrease as a function of principal tensile strain. The occurrence of punching failure is characterised by the out-of-plane shear stiffness approaching zero. Although the model can predict punching failure reasonably well, the results are very sensitive to the assumed cracked shear modulus [4]. Overly large values of cracked shear modulus lead to punching capacity being overestimated and in the limit to flexural rather than shear failure.

A recent study by Hrynyk and Vecchio [6] extended the model of Polak [4] by employing the disturbed stress field model (DSFM) of Vecchio [7]. The main difference between the MCFT and the DSFM is that the latter considers discrete slip on crack surfaces in the formulation of strain compatibility. Another modification to [4] is the adoption of a parabolic strain variation through the

plate thickness. This leads to better predictions of out-of-plane shear capacity for shear-critical elements, especially for members without out-of-plane shear reinforcement. Both models [4,6] have the drawback of not explicitly modelling post-punching behaviour which controls the global failure of flat slab systems with multiple slab-column connections.

In the second shell element modelling approach, punching shear failure is modelled with additional beam or joint elements which are positioned around the punching control perimeter. This technique was successfully employed by Keyvani et al. [8] to investigate the progressive collapse of laterally-restrained flat slab systems. Connector elements were used around the punching control perimeter to model the separation of the slab from the column at punching failure. The connectors comprised three dimensional Cartesian-Cardan connector elements with six degrees of freedom. The out-of-plane shear resistance of the connectors was calculated using the critical shear crack theory (CSCT) of Muttoni [9]. The post-punching capacity was modelled explicitly with additional connector elements which were used to connect the tensile and integrity reinforcement bars to the slab on either side of the critical shear crack. The connector strength was determined using the model of Mirzaei [10]. Although the model produces accurate predictions of both pre- and post-peak behaviour, the punching shear resistance of the connector elements needs to be determined prior to the global analysis without consideration of the slab kinematics during loading. This procedure can be inaccurate for continuous slabs where inwards movement of the line of radial contraflexure, subsequent to reinforcement yielding at supports, can increase punching resistance [3].

Recently, Liu et al. [11,12] used a similar procedure, but with two beam connector elements per column side, to study the progressive collapse of flat slab buildings. The beam element used six uncoupled degrees of freedom to simulate flexure, torsion, shear, and axial components within the critical punching region. Simarly to [8], this study used the CSCT failure criterion but no post-punching resistance is assumed. On failure, the connector beams immediately separate from the slab on the side where punching failure initiates. This neglects the benefit of shear redistribution of the type identified by Sagaseta et al. [13] which can significantly enhance the punching resistance particularly when loading or geometry is non-axis-symmetrical. Furthermore, when used to assess global behaviour, the shear capacity and failure rotation of each connector element was pre-determined from the intersection of the CSCT failure criterion with the load rotation response of a concentrically loaded isolated specimen with radius equal to the line of elastic contraflexure. As acknowledged by Liu et al. [11,12], this treatment neglects the increase in punching resistance which occurs as the line of contraflexure moves in towards the column, producing a stiffer response, as the slab is loaded beyond cracking and yielding.

Solid finite elements have been used for modelling punching failure since the early 1980s. One of the earliest studies was that of Yamazaki and Hawkins [14] who used elastic 3D-solid elements as well as nonlinear plate bending elements to study moment transfer at internal slab-column connections. The study showed that nonlinear plate bending analyses can provide reasonably accurate estimates of the

distribution of shear, moment, and torsion acting on "*finite areas of a connection transferring moment between a slab and a column*".

Recently, Genikomsou and Polak [15] carried out a comprehensive finite element investigation of punching shear employing 3-D solid elements in ABAQUS. The study examined interior and exterior slab-column connections under both static and reversed-cyclic loading. Concrete was modelled using a concrete damage plasticity model in compression and the fictitious crack model of Hillerborg et al. [16] in tension. Genikomsou and Polak showed that the accuracy of the finite element predictions was most influenced by the choice of dilation angle and damage parameters. They showed that 3-D finite element analysis is capable of producing accurate predictions of punching capacity, deflection and crack patterns. A recent study by Shu et al. [17] shows that finite element analysis with 3-D solid element can also be used to provide detailed information on the shear stress distribution along the control perimeter as well as radial and tangential strain in the concrete surface near supports. The study showed that finite element modelling with 3-D solid elements is capable of producing accurate and, more importantly, consistent results for the punching resistance of slabs with various geometries, reinforcement arrangements, support types, and loading arrangements. Similar conclusions have been reached by others [18-20].

This work presents a novel numerical methodology for using joint elements to simulate punching shear failure in RC slabs modelled with nonlinear layered shell elements. Only slabs without shear reinforcement are considered here, but the procedure will be extended in a future article to include shear reinforcement. The failure criterion of the CSCT [9] is used to determine the shear resistance of individual joint elements due to its accuracy and robustness. The joint elements incorporate a novel procedure for monitoring the slab rotation at user defined positions throughout the analysis. This allows the joint strength calculated with the CSCT to be continually updated throughout the analysis as the slab rotation changes, thereby avoiding the need to pre-define the punching resistance of connector elements as done in previous studies [8, 11, 12]. The proposed approach explicitly considers the influence on shear failure of shear redistribution, membrane action, cracking and reinforcement yielding. Additionally, post-punching resistance is modelled explicitly making it possible to simulate progression of failure in global building models. The procedure is shown to be capable of accurately simulating punching shear failure of isolated internal RC slab-column connections tested to failure under various loading arrangements and slab edge boundary conditions.

2 Proposed numerical methodology

2.1 General overview

The proposed approach simulates punching failure using joint elements positioned around a rectangular control perimeter, located at $d/2$ from the column face (where d is the slab effective depth). Local joint failure occurs when the joint shear force reaches the joint shear resistance

calculated with the CSCT. After initial failure, the joint strength is assumed to soften in accordance with the CSCT allowing additional load to be redistributed to adjacent slab sectors as proposed by Sagaseta et al. [13]. The post-peak punching resistance is calculated with the mechanical model of Fernandez Ruiz et al. [21]. The proposed modelling strategy is computationally efficient making it suitable for global analysis of structures. In addition, analysis of the internal joint forces also gives valuable insights into shear redistribution and the contribution of eccentric shear to moment transfer between slab and column.

2.2 RC layered-shell formulation and material parameters

The proposed joint model is implemented in the nonlinear structural analysis program ADAPTIC [22] within which the slab is modelled using a layered-shell element based on the conventional Reissner-Mindlin hypothesis. Full details of the shell element formulation and concrete material modelling are given elsewhere by Izzuddin et al. [23] so only a brief description is given here. The following assumptions are made in the shell element formulation:

1. Plane sections remain plane after deformation, but not necessarily normal to the element mid-surface;
2. Out-of-plane stresses are negligible;
3. Concrete cover depth is uniform;
4. Steel reinforcement is modelled as an equivalent uniform thickness plate acting uniaxially along a specified direction;
5. Only in-plane reinforcement is considered;
6. Perfect bond is assumed between concrete and reinforcement.

A layered approach is used to account for the nonlinear variation of material stress. Each shell element is discretised into a specific number of layers through its thickness. An initial sensitivity study in which 10, 15 and 20 layers were adopted through the shell thickness showed that 10 layers is sufficient to capture the slab load-rotation response accurately. Thus, in this study, all reported analyses were carried out using 10 layers through the slab thickness. Both geometric and material nonlinearity are considered within the shell element formulation. Geometric nonlinearity is allowed for by using the corotational formulation proposed by Izzuddin [22, 24]. The concrete material model considers the influence of both tensile cracking and compressive nonlinearity, including softening effects. Nonlinearity is limited to the biaxial planar stress with out-of-plane behaviour assumed to be linear elastic. A correction factor of 5/6 is applied to relate out-of-plane shear strains to out-of-plane shear stresses on account of the actual shear stress distribution being closer to parabolic than uniform as assumed [23]. A fixed crack model is used in which the crack direction is determined by the principal stress direction at the moment of crack initiation. A shear retention factor (β_s) is used to

reduce the in plane shear stiffness after cracking occurs. Under compression, concrete material nonlinearity is modelled using an evolving plastic interaction surface in the biaxial plane. Tensile softening of concrete is modelled by means of a separate strength envelope for the biaxial stresses ($\sigma_{xt}, \sigma_{yt}, \tau_{xyt}$) which is expressed as a function of crack strains ($\varepsilon_{xc}, \varepsilon_{yc}$). The slope of the tension softening curve a_t defines the crack strain at which the tensile stress reduces to zero and hence the level of tension stiffening. Reinforcement is modelled with equivalent uniaxial plates of uniform thickness assuming perfect bond and a bilinear stress strain curve with minimal strain hardening.

2.3 Constitutive behaviour of joint element

The 6-degree of freedom 3D joint element *jel3* [22, 25] is used to simulate punching shear failure. Each *jel3* element consists of two coincident nodes (nodes 1 and 2 in **Figure 1**). The element accounts for geometric nonlinearities and incorporates independent nonlinear force-displacement relationships for each DOF (uncoupled behaviour). This implies that the local tangent stiffness is always a diagonal matrix, with the diagonal terms corresponding to the force-displacement curve of the corresponding degree of freedom. As shown in **Figure 1(a)**, two additional nodes (depicted nodes 3 and 4), which can be either structural or non-structural, are used as references for the local axes. The local x axis is initially defined by a vector connecting nodes 1 and 3 while the local y-axis lies in a plane defined by the local x-axis and node 4. At each load step, the orientation of the local axes is updated using the increments in global rotations at node 1 as shown in **Figure 1(b)**. Deformation of the joint element is represented by separation of nodes 1 and 2, in term of local translational and rotational displacements (see **Figure 1(b)**). In this study, node 3 is positioned at the slab rotation monitoring point and node 4 is positioned on the column chord above the slab. The relative slab-column rotation, which is needed in the CSCT, is obtained from the difference in rotation of nodes 3 and 4. In this work, all local DOFs, except out-of-plane translation are modelled as fully rigid.

Joint elements are uniformly spaced around the control perimeter as shown schematically in **Figure 2(a)**. Each joint element has a sector element associated with it. The location at which rotations are monitored is chosen by the analyst. For best fit with experimental observations, sector rotations are monitored in this paper at a radius of $0.2L$ from the column centreline (where L is the slab span between column centrelines) as recommended by Soares and Vollum [20] who showed that the rotation remains almost constant over a significant distance from the column. However, in general, the monitoring point should be positioned where the relative slab-column rotation is a maximum. It is necessary to monitor rotations remote from the joint because the deflected shape obtained with shell elements is more rounded adjacent to the column than observed in laboratory tests [20, 26]. In a continuous slab, the radius of $0.2L$ corresponds to the line of radial contraflexure under axisymmetric loading. In isolated internal slab-column test specimens, the radius of $0.2L$ was taken as half the slab

width. In accordance with the CSCT failure criterion [9], the mean punching shear resistance of each joint element V_{cap} is calculated as follows in terms of its sector rotation ψ_s:

$$V_{cap} = \frac{V_R}{n} = \frac{0.75 b_{0,3d} \,.\, d \,.\, \sqrt{f_c'}}{n\left(1 + 15\,\frac{\psi_s \,.\, d}{d_{g0} + d_g}\right)} \qquad (1)$$

where V_R is the punching resistance of an axisymmetric slab with uniform rotation ψ_s, d is the average slab effective depth and $b_{0,3d}$ is an effective control perimeter with rounded corners at $d/2$ from the column face. The length of the straight segments of $b_{0,3d}$ is limited to a maximum of $3d$ for each side of the column. n is the number of joint elements around $b_{0,3d}$, f_c' is the concrete compressive strength, d_g is the maximum aggregate size, and d_{g0} is a reference aggregate size equal to 16mm.

For the idealised axisymmetric slab shown in **Figure 2(a)**, the resulting failure load is the same as given by the CSCT but this is a special case since in general neither the rotation nor shear force distribution are uniform around the control perimeter. Three phases of behaviour are considered for the out-of-plane DOF as described below and shown in **Figure 2(b)**. It should be noted that the joint shear force is related to the vertical sliding displacement of the joint (between node 1 and 2) in Stages I and III but to the slab rotation, via the joint shear resistance, in Stage II.

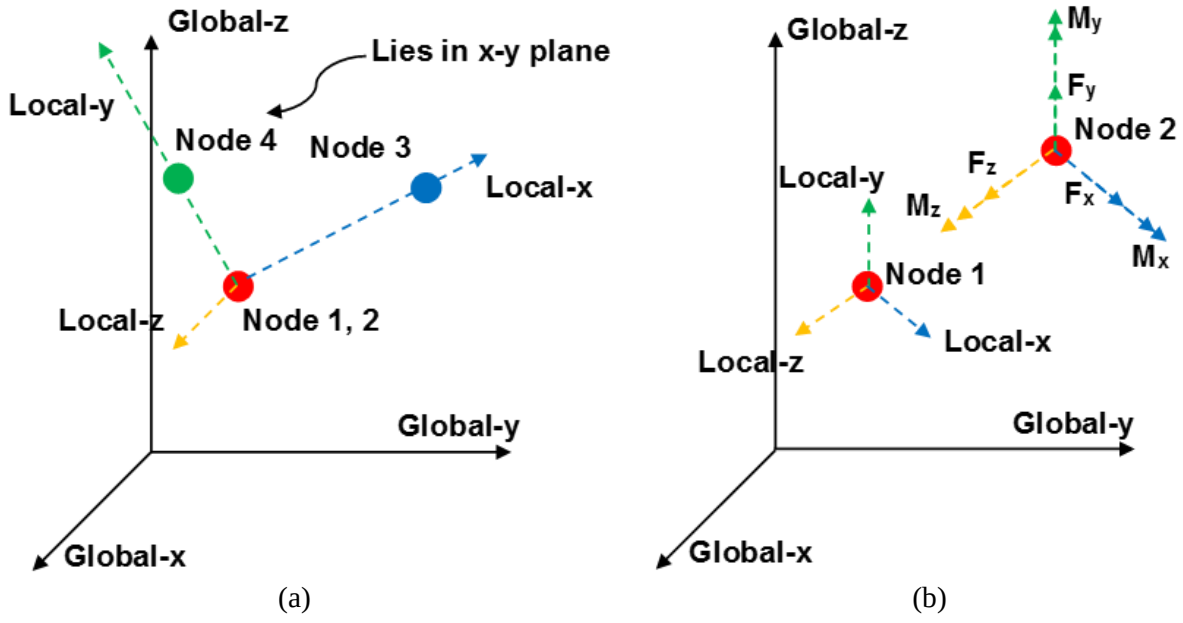

Figure 1. Configuration and local force components for joint element (*jel3*): (a) before and (b) after joint deformation

- **<u>Stage I (ascending branch – initial phase)</u>**

  Although the joint element used here is of zero-length, it is still necessary to assume a notional spring length in order to derive the out of plane displacement stiffness parameter. For this purpose, the

notional joint length is assumed equal to the slab thickness giving rise to an equivalent shear strain of $\gamma = \delta/t$ where δ is the vertical joint separation and t is the slab thickness. Initially, the joint element is assumed to behave linearly with out of plane displacement stiffness (k_{inc}) formulated as:

$$k_{inc} = k_{red} \cdot \frac{E_c}{2(1+\nu)} . l_s \quad (N/mm) \tag{2}$$

where ν is Poisson's ratio for concrete which is taken as 0.2, E_c is concrete elastic modulus, k_{red} is a joint stiffness reduction factor and l_s is the spacing between adjacent joint elements.

Calibration studies (see **Section 3.5**) showed that a suitable value for the joint stiffness reduction factor k_{red} in **Equation 2** is 0.1 as used in the shell element for reduction of in-plane shear stiffness after cracking. Taking k_{red} = 0.1, which was used in all the presented analyses, makes the joint elements sufficiently stiff to prevent unrealistic slab vertical separation before global punching failure is triggered. Increasing k_{red} above 0.1 can overestimate the proportion of unbalanced moment resisted by eccentric shear thereby causing premature punching failure as shown in **Section 3.5**. Each joint behaves linearly until its load rotation response first intersects the CSCT failure criterion. Subsequently, the joint response is described by Stage II.

- **Stage II (softening branch – redistribution phase)**

  After initial failure, the joint shear force equals the joint shear resistance calculated with the CSCT using the monitored slab rotation. This results in shear force being redistributed from failing joint elements to joint elements yet to fail. In Stage II, the individual joint shear resistance at load step *i* is calculated according to the CSCT failure criterion. Thus, the post-peak joint relative vertical displacement depends on the slab rotation at the monitoring point and is independent of the column penetration (joint vertical separation). Consequently, the column penetration is determined internally within ADAPTIC as a function of the joint forces.

- **Stage III (post-punching branch – global failure phase)**

  Subsequent to failure of all joints, the vertical joint separation increases significantly since it is no longer restrained by joints yet to fail. In this study, Stage III was triggered by a relative joint deformation of 1 mm in the global-z direction. The choice of 1 mm is somewhat arbitrary but has no influence on the Stage III residual post-peak punching capacity of isolated slab column specimens. The choice of triggering displacement may play a more important role in the modelling of complete floor systems where delaying failure at one connection directly affects the behaviour of adjacent slab-column connections. However, this is the subject of ongoing research, outside the scope of this paper, in which a rational basis is being developed for the selection of the displacement at which Stage III is triggered. The Stage III joint resistance reduces linearly with slope k_{deg} (Stage III-a) until the post-

peak resistance is reached after which the resistance remains constant. The choice of k_{deg} is discussed in **Section 3.3.4**. The post-peak resistance (V_{pp}) is predetermined using the mechanical model of Fernandez Ruiz et al. [21] which accounts for the contributions of the top and bottom (integrity) reinforcement crossing the punching cone while limiting the maximum strength to the concrete pull-out strength.

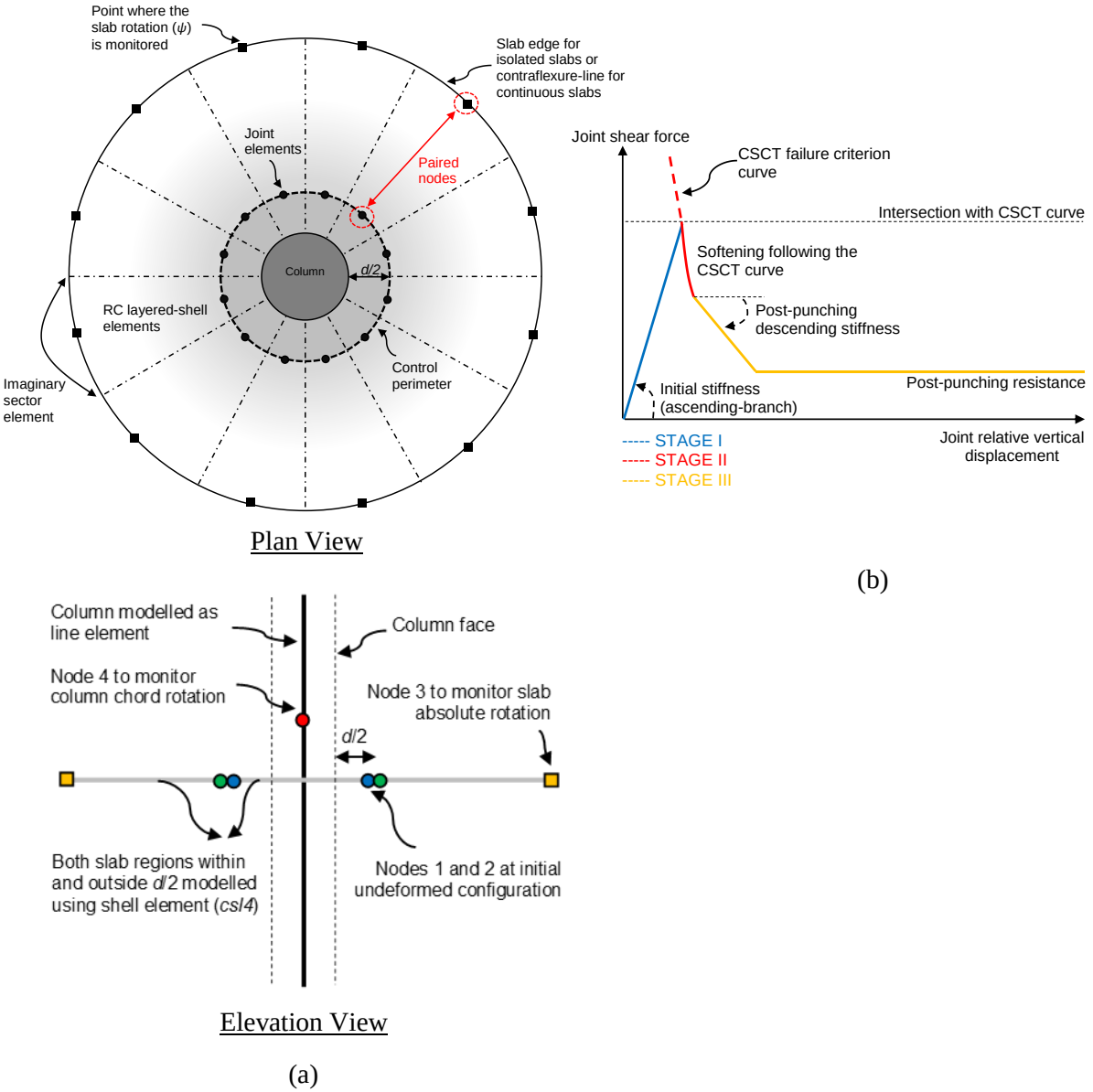

Figure 2. **(a) Illustration of the proposed methodology; (b) Joint constitutive relationship for out-of-plane DOF.**

The flowchart in **Figure 3** illustrates the solution procedure used to determine joint shear resistance and connection punching failure in ADAPTIC.

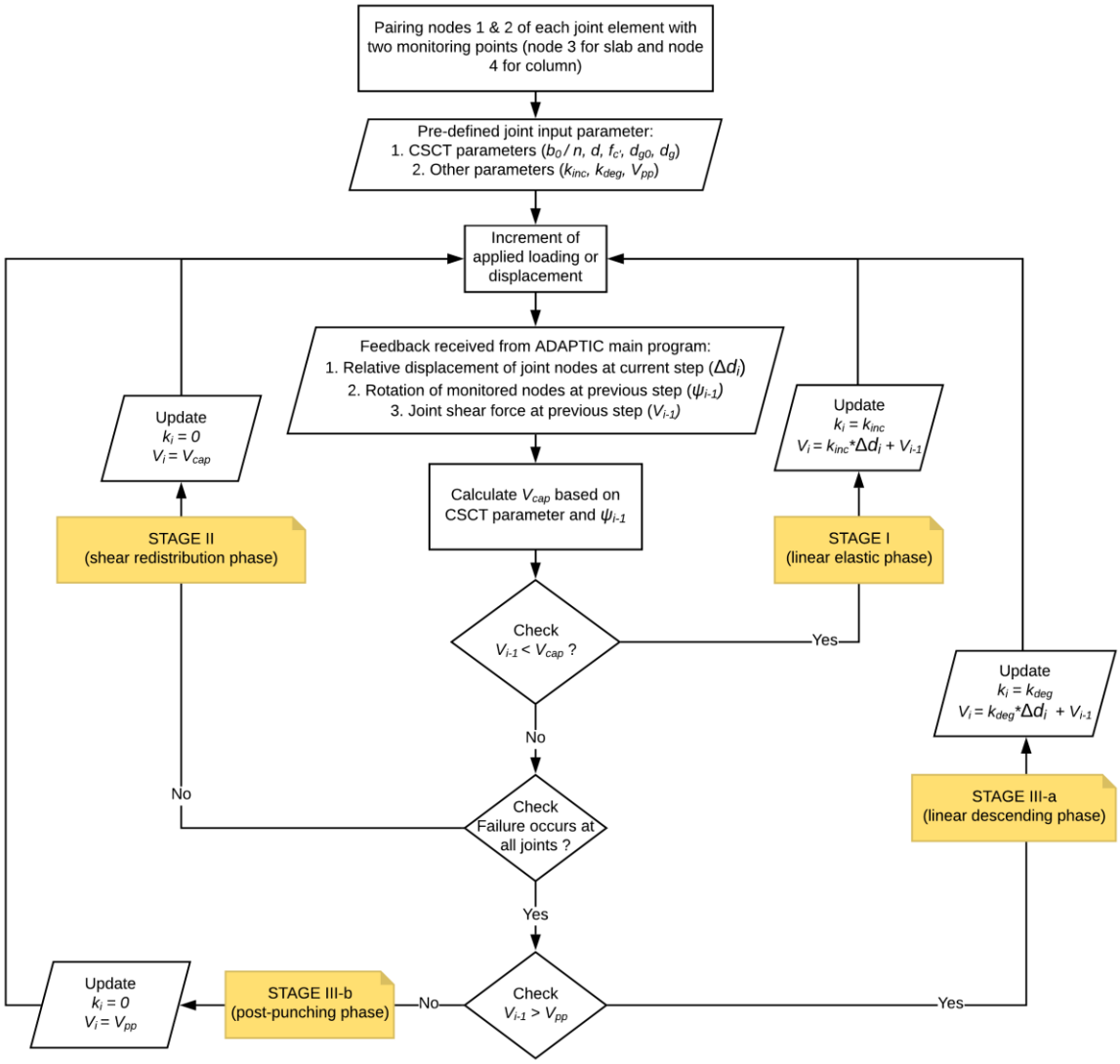

Figure 3. Algorithm of the joint model implemented in ADAPTIC.

2.4 3-D solid modelling with ATENA

For comparison with the proposed shell model, 3-D modelling was also carried out with the finite element code ATENA [27]. In ATENA, a fully rotating smeared crack approach was used in conjunction with concrete material model CC3DNonLinCementitious2 which combines constitutive models for tensile (fracture) and compressive (plastic) behaviour. The Rankine tensile failure criterion was used with exponential softening. Plasticity for concrete in compression is controlled by the Menetrey-Willam failure surface [28]. The hardening part of the compressive response is expressed in terms of strain, while the softening part is expressed in terms of displacement to introduce mesh objectivity into the finite element solution. The shape of the compressive softening response is based on the work of Van Mier [29]. After concrete cracks, the compressive strength in the direction parallel to the cracks is reduced similarly to the MCFT [5]. However, in ATENA, this relationship is

described by Gauss's function which allows the user to flexibly adjust the effect. Linear order (8-noded) brick elements were used to model the slabs. Calibration studies showed that the out-of-plane shear behaviour of the slabs could be captured accurately using 10 brick elements through the slab thickness. Perfect bond was assumed between reinforcement and concrete. **Table 1** summarises the material parameters and loading procedure used in the all the analyses. Parameters A1 to A3 are default values calculated internally within ATENA in terms of the concrete compressive strength. No attempts were made to improve the results of individual analyses.

Table 1. Summary of material parameters and loading procedure for NLFEA in ATENA.

No.	Parameter	Value/Reference
	Concrete constitutive model	
A1	Concrete elastic modulus	fib Model Code 1990 recommendation [30]
A2	Fracture energy	fib Model Code 2010 [31]
A3	Concrete tensile strength	fib Model Code 2010 [31]
A4	Smeared crack model	Fully-rotating crack
A5	Critical compressive displacement	0.5 mm
A6	Limit of compressive strength reduction due to cracking (MCFT)	$0.8f_{c'}$
A7	Eccentricity (defining the shape of the failure surface)	0.52
A8	Volume dilatation plastic factor	0
	Reinforcement bar model	
B1	Stress-strain relationship	Bilinear
B2	Bond-slip model	Perfect bond
	Loading procedure and convergence criteria	
C1	Loading procedure	Static (force-controlled)
C2	Iteration method	Arc-length method
C5	Convergence criteria for displacement, residual, and absolute residual error	1%
C6	Convergence criteria for energy error	0.1%
	Mesh properties	
D1	Number of finite elements through the slab thickness	10
D2	Mesh element for concrete slab	8-noded hexahedral (linear)
D3	Mesh element for loading apparatus	4-noded tetrahedral (linear)
D4	Mesh element for reinforcement bar	2-noded truss element (embedded)

3 Verification of joint model

3.1 Calibration of material parameters and mesh discretisation for shell model

The material input parameters for the shell model and mesh discretisation were derived in an initial study in which joint elements were omitted. The study developed a modelling procedure capable of capturing the load-deformation response accurately from first load to flexural failure as required for accurate implementation of the CSCT. The following internal slab-column tests were modelled in the initial calibration without joint elements:

1) 3 axisymmetric tests: two from Sagaseta et al. [13] and one from Guandalini et al. [32];
2) 2 non-axisymmetric tests from [13];
3) 4 slabs loaded with constant eccentricity and increasing shear force from Hawkins et al. [33];

4) 5 slabs loaded with constant shear force and increasing eccentricity from Drakatos et al. [34].

Taking advantage of symmetry, one quarter of the slab was modelled in cases 1) and 2) and half of the slab in cases 3) and 4). Quadrilateral elements with linear order (4 nodes) were used for all models as shown in **Figure 4(a)**. Each shell element was discretised into 10 layers through the slab thickness with each layer containing 2 × 2 Gauss points. The mesh discretisation varied between the specimens, but was sufficiently fine in all cases (around 50-100 mm mesh size) in order to allow for the subsequent insertion of a minimum of three joint elements along each half side of the control perimeter as indicated in **Figure 4(b)** which also shows the nodes where slab rotations were monitored. Point loads were applied to the node closest to the centre of load application in the test. Static analysis was used to simulate the actual test protocol. Initially, force-control was used with Newton-Raphson method but at later loading stages this was changed to displacement-control with Arc-length method in order to capture the post-peak response. The preliminary studies showed that the load-rotation response of the considered slabs is well captured using the ADAPTIC material input properties summarised in **Table 2**. Default compressive concrete properties for con11 (A4, A6, A8 and A9 in **Table 1**) are taken from Elghazouli and Izzuddin [35]. Property A5 was taken as 0.4 compared with 0.2 in [35] but parametric studies show the results to be insensitive to this change. The shear retention factor β_s was taken as 0.1 which is in the commonly suggested range [36] but the results are insensitive to this choice. For consistency with the 3-D nonlinear finite element modelling with ATENA [27] (see **Section 2.4** and **Table 1**), the concrete elastic modulus (E_c) was calculated in accordance with fib Model Code 1990 [30] while the concrete tensile strength (f_t) was calculated in accordance with fib Model Code 2010 [31]. As suggested by Vollum and Tay [37], the concrete tensile strength was reduced to $0.5f_t$ in ADAPTIC with the softening slope a_t chosen to reduce the tensile stress linearly to 0 at a strain of $\varepsilon_{ft0} = 0.001$. This combination of parameters was chosen [37] to give a best fit to deflections calculated with EC2 [2]. It results in good estimates of measured deformations as shown in **Figure 5** for slab PT22 from Sagaseta et al. [13] as well throughout the paper in the presented load-rotation plots. **Figure 5** illustrates the sensitivity of the calculated deflection to a) the adopted concrete tensile strength for $\varepsilon_{ft0} = 0.001$ and b) varying ε_{ft0} with adopted tensile strength of $0.5f_t$. Linearly reducing the tensile stress resisted by cracked concrete to zero at a strain of $\varepsilon_{ft0} = 0.001$ avoids increasing flexural resistance, due to residual tensile stress at cracks as indicated in **Figure 5(b)**. The same modelling parameters were used in the verification of the FE model with joint elements.

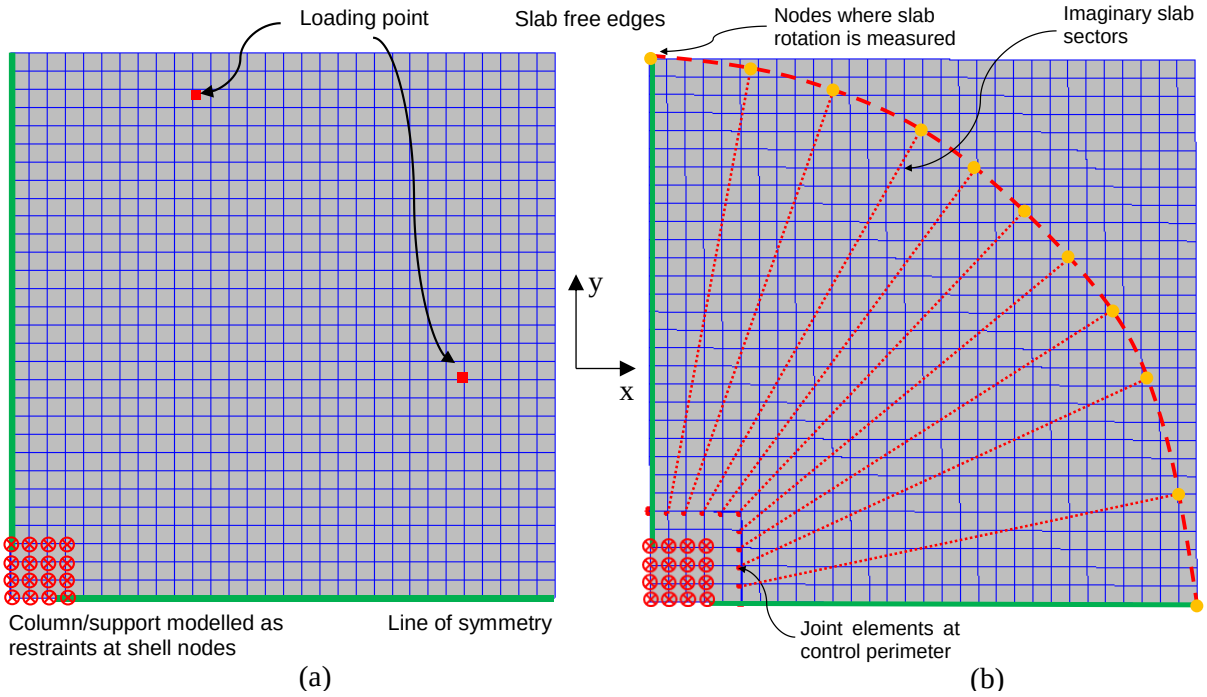

Figure 4. **Plan view of mesh discretisation and boundary conditions for typical slab modelled in ADAPTIC: (a) pure shell element model; (b) proposed model combining shell and joint elements.**

Table 2. **Calibrated material parameters for shell element from preliminary study.**

No.	Parameter	Value/Reference
	Concrete constitutive model	
A1	Smeared crack model	Fixed crack
A2	Poisson's ratio	0.2
A3	Tensile softening slope (a_t)	f_t / *0.001*
A4	Normalised initial compressive strength (s_c)	0.4
A5	Normalised residual compressive strength (r_c)	0.4
A6	Factor for biaxial compressive interaction (b_c)	0.6
A7	Elastic shear retention factor (β_s)	0.1
A8	Factor scaling direct tensile stresses for shear interaction (ϕ_s)	0.4
A9	Normalised shear softening relative to direct tensile softening (γ_s)	0.0
	Reinforcement bar model	
B1	Stress-strain relationship	Bilinear
B2	Ratio of post-yield / elastic stiffness	0.00001 (elasto-plastic)
B3	Bond-slip model	Perfect bond

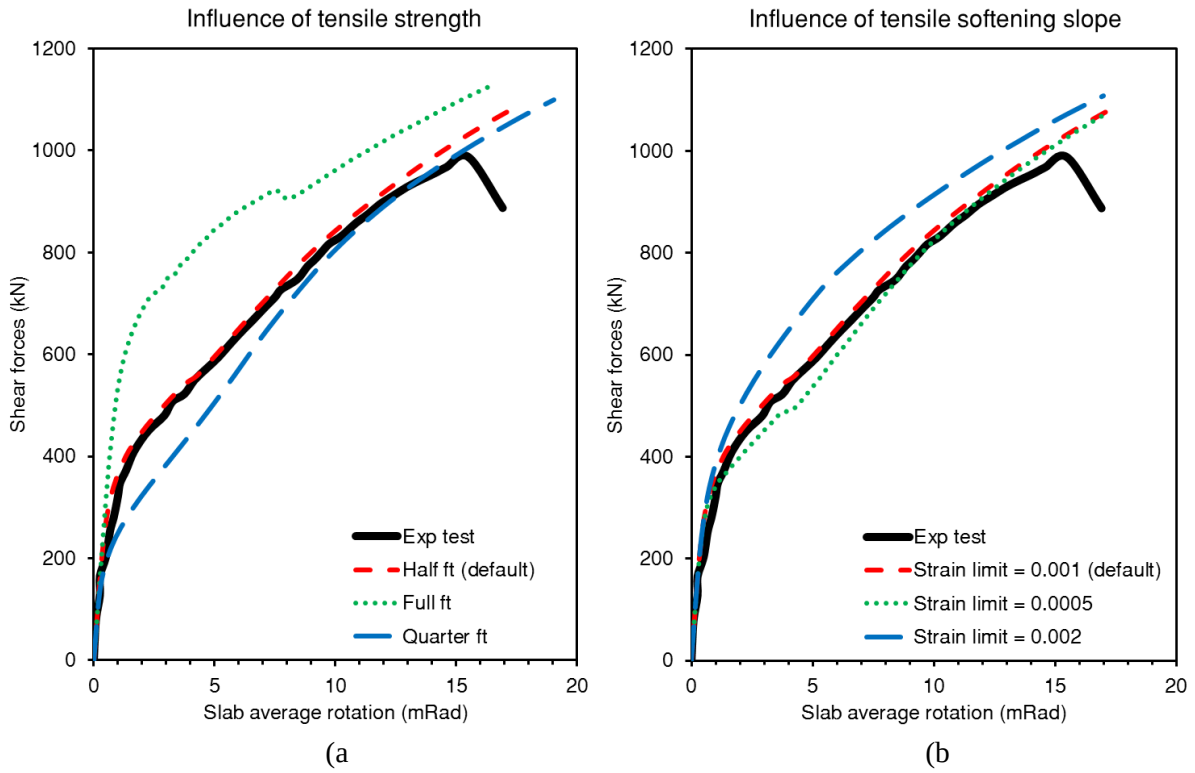

Figure 5. **Influence on deflection of slab PT22 [13] of: (a) concrete tensile strength with limiting strain of 0.001; (b) influence of limiting strain for concrete tensile strength of 0.5f_t.**

3.2 Assessment of joint model using test data

The proposed modelling procedure was verified by modelling isolated punching shear tests from the literature with the following loading and boundary conditions:

1) Axisymmetric

a) Influence of flexural reinforcement ratio: 5 slabs
b) Influence of size effect: 5 slabs
c) Influence of in-plane compressive forces: 6 slabs
d) Post-punching behaviour: 4 slabs

2) Non -axisymmetric

a) Non-symmetric reinforcement or loading configuration: 5 slabs
b) Elongated column: 6 slabs

3) Eccentrically loaded

a) Constant eccentricity; increasing shear force: 11 slabs
b) Increasing eccentricity; constant shear force: 5 slabs

Each series of tests is discussed separately in **Sections 3.3** to **3.5** which include representative measured and predicted load-deformation plots. Detailed results for all the analysed slabs are presented in **Table 3** which is discussed in **Section 3.6**.

3.3 Category 1: Axisymmetric

3.3.1 1a) Influence of flexural reinforcement ratio

The following five internal slab-column specimens, having three different reinforcement ratios, were modelled:

a) PG-5 from Guandalini et al. [32] with 0.33% flexural reinforcement ratio (ρ_{top});
b) PT22 from Sagaseta et al. [13] and PG19 from Clement et al. [38] both with reinforcement ratio around 0.80%;
c) PT31 from [13] and PG20 from [38] both with reinforcement ratio around 1.50%

All five slabs had similar geometry and test setup. The slabs, which measured 3000 mm × 3000 mm × 250 mm, were centrally supported on a 260 mm square steel plate and loaded concentrically at eight points positioned at a radius of 1500 mm from the slab centre. **Figure 6** shows load-rotation responses for the selected slabs obtained with the proposed methodology, ATENA and experimentally. In addition, the mean CSCT failure criterion [9] is also shown for comparison. The CSCT failure load is given by the intersection of the load rotation and resistance curves. **Figure 6** shows that the proposed approach gives conservative estimates of punching resistance which are almost identical to those obtained graphically from the intersection of the calculated load rotation response and the CSCT failure criterion. **Figure 6(a)** compares the measured and predicted responses of PG-5 where "*punching failure occurred with large plastic deformations at the onset of the yield-line mechanism*" [32]. The figure demonstrates that the proposed model is able to simulate punching failure when it occurs subsequent to yielding of flexural reinforcement as in lightly reinforced slabs. The shapes of the experimentally observed post-peak load rotation responses shown in **Figures 6(b)** and **6(c)** are not considered significant. In both cases, punching failure was brittle with the post-peak response dependent on the adopted loading protocol. The snap back response obtained with the proposed joint method is a result of the adopted displacement-control with Arc-length iteration solution procedure. In the analysis, the post-peak rotation reduces as a result of the slab unloading while the vertical displacement increases due to joint separation. For these slabs, the ATENA predictions are especially accurate and better than the CSCT predictions.

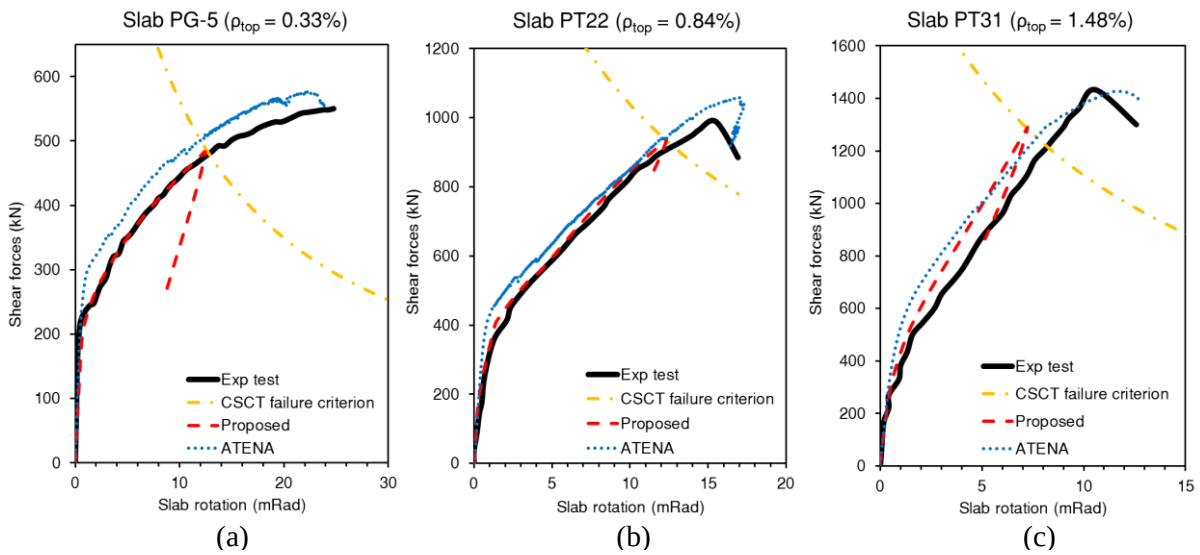

Figure 6. Load-rotation response and failure point of selected slabs with flexural reinforcement ratio of: (a) 0.33%; (b) 0.84%; and (c) 1.48%.

3.3.2 1b) Influence of size effect

The capability of the joint model to simulate the so called "size effect" was verified by modelling the following five half, normal and double size test specimens of Guandalini et al. [32]:

a) Half-size (1500 mm × 1500 mm × 125 mm): PG-6 and PG-7
b) Normal-size (3000 mm × 3000 mm × 250 mm): PG-1 and PG-11
c) Double-size (6000 mm × 6000 mm × 500 mm): PG-3

The test setup for this series was the same as described in **Section 3.3.1**. **Figure 7** shows, for the selected slabs, experimental and predicted slab edge deflections at loading points. The proposed joint model is seen to broadly capture the experimental load-deflection response and failure load for all three slab sizes. This is to be expected, since the CSCT failure criterion takes into account the so called "size effect" implicitly within its formulation. The presented ATENA predictions are also reasonable.

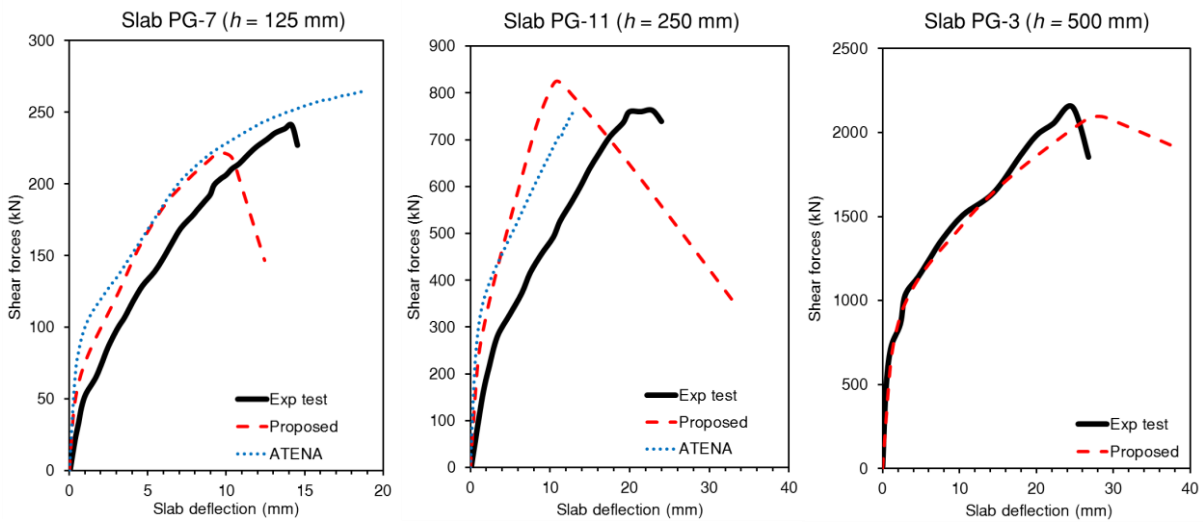

(a) (b) (c)

Figure 7. Load versus slab edge deflecton of selected slabs with slab thickness of: (a) 125 mm; (b) 250 mm; and (c) 500 mm.

3.3.3 1c) Influence of in-plane compressive forces

The ability of the joint model to simulate the influence of in-plane compressive force was investigated by modelling three pairs of punching specimens tested by Clement et al. [38]. Two different mechanisms of punching shear enhancement occur in slabs with compressive in-plane forces as discussed by Clement et al. [38]. The first results from the decrease of slab rotation caused by in plane axial force. This is directly accounted for in the ADAPTIC analysis through the axial-bending interaction of the shell element formulation. The second mode of shear enhancement results from the increased depth of the flexural compression zone due to pre-stressing. This factor can be considered by enhancing the resistance provided by the CSCT failure criterion. In the FE analysis, this was done by using the reduced rotation proposed by Clement el al. [38] (ψ') instead of the actual monitored slab rotation (ψ) when calculating the joint shear resistance. The slabs in each pair were reinforced with 0.75% and 1.50% hogging reinforcement. The average in-plane compressive stress was varied as follows:

a) PC9 and PC10 with edge compressive stress of around 1.25 MPa
b) PC5 and PC6 with edge compressive stress of around 2.50 MPa
c) PC7 and PC8 with edge compressive stress of around 5.0 MPa

The slab geometry and test setup of these slabs were the same as described in **Section 3.3.1** apart from the pre-stressing force which was introduced at slab edges before the gravity load was applied. For this test series only, the input rotation to the CSCT failure criterion was refined as follows in accordance with the suggestion of Clement et al. [38]:

$$\psi' = \psi + 45\left(\frac{\sigma_n}{E_c}\right) \geq 0 \qquad (3)$$

where σ_n is the applied average compressive membrane stress (- sign for compression).

The refined rotation ψ' accounts for the depth reduction of the cracked zone due to pre-stressing which also reduces the crack width for a given rotation [38]. No modification is required to the load-rotation response since the shell element formulation itself accounts for the interaction between bending and compression actions. The load-rotation response of selected slabs with various edge compressive stress acquired with the proposed approach is plotted in **Figure 8** along with the original [9] and refined [38] CSCT failure criteria. The joint model gives good estimates of the failure load, even though the predicted load-rotation response is overly stiff. The explanation for this is provided by Clement et al. [38] who write "*For the test setup of series N, however, a second order moment appears due to the deflection of the slab (the external prestressing being thus applied with an eccentricity)*". Furthermore, according [38], "*This particular effect can nevertheless be neglected in the investigated tests and will not be considered in the following (differences in the failure load are lower than 3% for test series N)*". The difference in the measured and predicted initial responses arises because the prestressing force was assumed to act at the slab centre in the ADAPTIC analyses (i.e. no eccentricity). It is unclear why the overall predicted response is stiffer than observed but as shown in **Figure 8** the overestimate of stiffness has relatively little effect on the failure load given by the CSCT which occurs at the intersection of the load rotation and resistance curves.

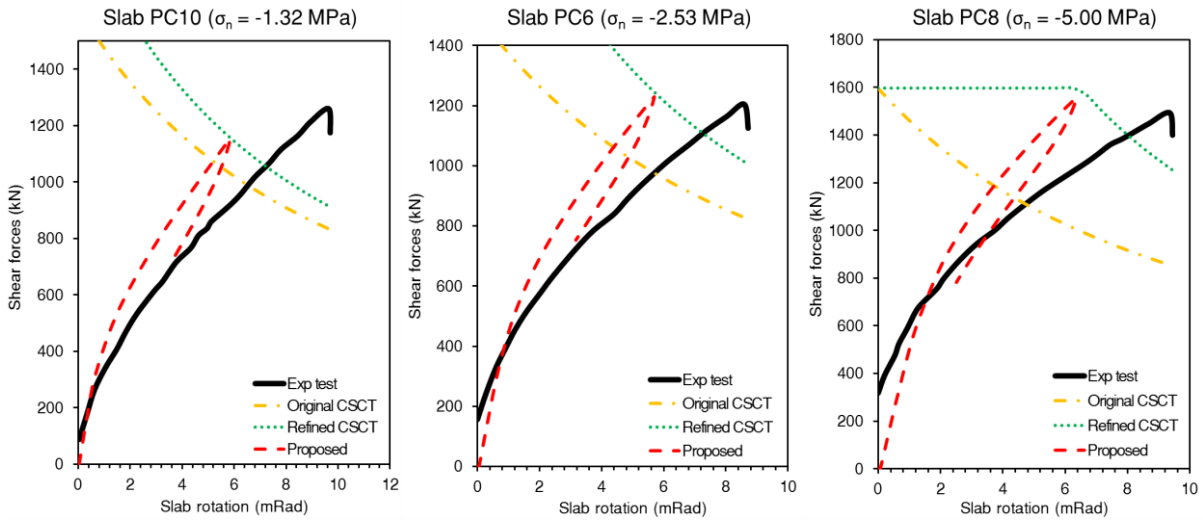

Figure 8. Load-rotation response and failure point of selected slabs subject to in-plane compressive stresses of: (a) 1.32 MPa; (b) 2.53 MPa; and (c) 5.00 MPa.

Figure 8 also shows that the use of ψ' in the CSCT failure criterion results in better predictions of the measured failure load than use of the actual rotation ψ. These analyses illustrate the capability of the proposed shell element formulation to simulate complex loading combinations and accommodate refinements to the failure criterion.

3.3.4 1d) Post-punching behaviour

The post-punching capability of the joint model was examined by modelling the following four punching specimens of Fernandez Ruiz et al. [21]:

a) PM3 and PM4 with only top flexural reinforcement bars (no integrity reinforcement)
b) PM9 with 4-D8 integrity reinforcement bars
c) PM10 with 4-D10 integrity reinforcement bars

These slabs were selected since they were part of an investigation into post-punching resistance. All the slabs measured 1500 × 1500 × 125 mm. The slabs were centrally loaded through a stiff steel plate measuring 130 × 130 mm and supported at a radius of 747 mm on eight steel plates which allowed sliding and rotation. **Figure 9** shows that the proposed approach captures the failure load and peak residual load capacity with reasonable accuracy. The tangent stiffness k_{deg} in Stage III (see **Figure 2**) was selected as -500 N/mm, with joint spacing of 25 mm, to match the observed load deflection response after punching (see **Figure 9**). Further research is required to generalise the calculation of k_{deg} but it does not affect the minimum post-peak resistance which was calculated using the model of Fernandez Ruiz et al. [21]. However, the choice of k_{deg} could affect the progression of failure in structures with multiple slab-column connections.

A more sophisticated resistance model is needed to capture the observed variation of post-peak resistance with displacement.

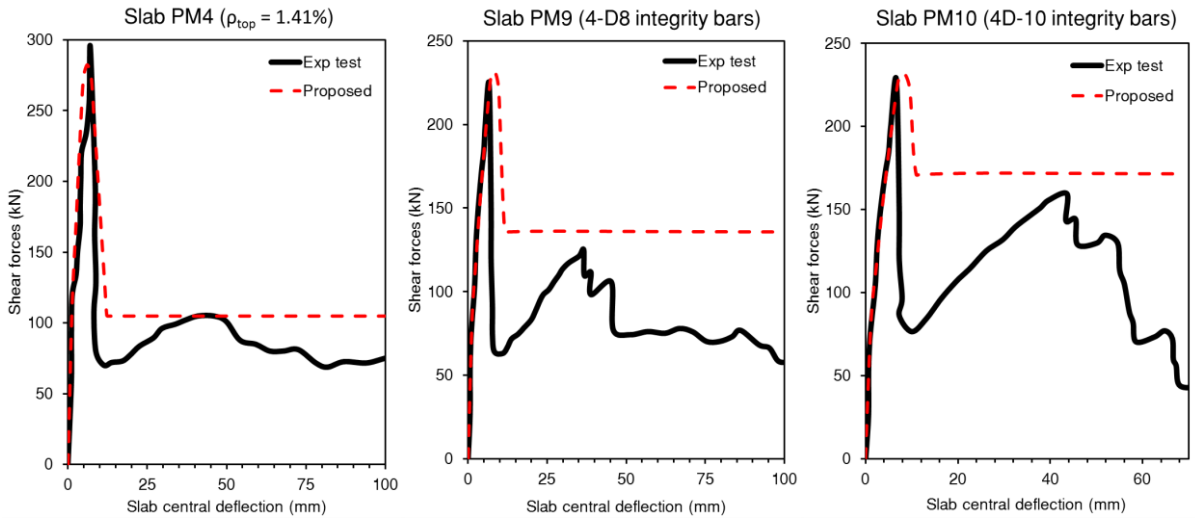

(a) (b) (c)

Figure 9. Load versus slab central deflection of selected slabs reinforced with: (a) only top reinforcement (no integrity bars); (b) 4-D8 integrity bars; and (c) 4-D10 integrity bars.

3.4 Category 2: Non-axisymmetric

3.4.1 2a) Non symmetric reinforcement and loading arrangement

The ability of the proposed approach to model non-axis-symmetric slabs was investigated by modelling all five of the slabs tested by Sagaseta et al. [13]. The slabs were either non-symmetrically reinforced or subjected to one-way bending as described below:

a) PT21 and PT32 had around 1.50% and 0.75% reinforcement ratio in x- and y- axis (ρ_x and ρ_y) respectively subjected to two-way loading

b) PT23 and PT33 had around 0.75% and 0.30% reinforcement ratio in x- and y- axis respectively subjected to two-way loading

c) PT34 had 0.75% symmetric reinforcement subjected to one-way loading

The slab and central support plate dimensions were the same as described in **Section 3.3.1**. The test set up was also the same except for slab PT34 where point loads were applied only on two opposite edges (parallel to the x-axis) to simulate one-way loading. An objective of reproducing this test series was to verify the capability of the proposed methodology to capture the additional punching strength provided by shear redistribution around the control perimeter [13]. **Figure 10** shows the comparison between the measured response and the predictions of the proposed methodology, 3-D solid elements, the CSCT and the so-called $V_{CSCT(\psi x\text{-}\psi y)}$ modification to the CSCT [13] (labelled as "modified CSCT

method") which takes into account shear redistribution. Rotations in **Figure 10** are shown about both the x and y axes.

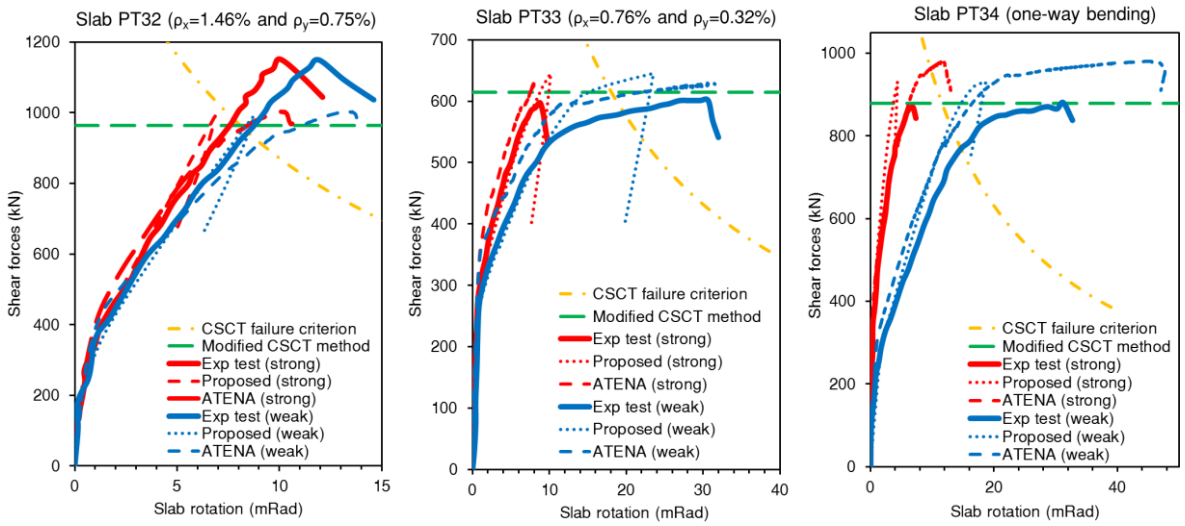

(a) (b) (c)

Figure 10. Load-rotation response and failure point of selected slabs with: (a), (b) two-way bending with different ρ_x and ρ_y; (c) one-way bending with symmetric reinforcement arrangement.

Figure 10 shows that the predictions of the joint model are in good agreement with those of the modified CSCT method of Sagaseta et al. [13]. The strength predictions of the joint model, the CSCT and the modified CSCT are similar for specimens PT32 and PT33 indicating that the influence of shear redistribution is minimal for these specimens. This is not the case for specimen PT34 in **Figure 10(c)** where both the joint model and modified CSCT yield higher values of strength than the CSCT due to shear redistribution. The predictions of the joint model also compare favourably with those of the 3-D ATENA model, which implicitly considers shear redistribution.

3.4.2 2b) Elongated column

The influence of column aspect ratio was investigated by modelling six slabs with ratio of longer to shorter column side (c_{max}/c_{min}) varying between 3 and 5. Details of the column aspect ratio and loading arrangement are given below:

a) AM01 and AM02 of Sagaseta et al. [39] with c_{max}/c_{min} = 3 and one-way loading applied on the slab edges parallel to the shorter column side
b) AM04 from [38] with c_{max}/c_{min} = 3 and two-way loading
c) L3c, L4c, and L5c of Olivera et al. [40] with c_{max}/c_{min} = 3, 4 and 5 respectively and two-way loading

Slabs AM01, AM02 and AM04 of Sagaseta et al. [39] measured 3000 mm × 3000 mm × 250 mm and were centrally supported on a rectangular column measuring 780 mm × 260 mm. The loading arrangement was as described in **Section 3.3.1**. Slabs L3c, L4c, and L5c of Olivera et al. [40]

measured 2280 mm × 1680 mm × 130 mm and were centrally supported on a rectangular column with shorter column side c_{min} equal to 120 mm in all tests. The slabs of Olivera et al. were symmetrically loaded through beams located close to the slab edges.

Joint elements were initially positioned around the full control perimeter of elongated columns but this was found to overestimate shear resistance (see **Figure 11**) as found by Sagaseta et al. [39]. Consideration was given to reducing the length of the control perimeter as done in MC2010 (see **Figure 12(a)**) but this was deemed unrealistic for slabs spanning one-way onto very elongated supports. Consequently, a minimum shear resistance was attributed to the straight lengths of the control perimeter neglected by MC2010 (V_{1_way}). In this study, the nominal one-way shear resistance per unit length is calculated using the following formulation of Cavagnis et al. [41] which is consistent with the CSCT:

$$v_c = \frac{k.d.\sqrt{f_c'}}{\sqrt{\varepsilon_s.\frac{d}{d_{dg}}}} \tag{4}$$

where k = 0.019 is an empirical coefficient [41], ε_s is the longitudinal reinforcement strain, and d_{dg} is the crack average roughness calculated as follows:

$$d_{dg} = \min(40\ mm, 16 + d_g) \quad \text{for } f_c' \leq 60\ MPa \tag{5a}$$

$$d_{dg} = \min\left(40\ mm, 16 + d_g * \left(\frac{60}{f_c'}\right)^2\right) \quad \text{for } f_c' > 60\ MPa \tag{5b}$$

where d_g refers to the maximum aggregate size.

Conservatively, the nominal one-way shear resistance used in the joint model is taken as that at first yielding of flexural reinforcement. The resulting joint shear resistance along the straight lengths of the control perimeter neglected by MC2010 [31] is given by:

$$V_{1\_way} = \frac{v_{c\_min}.\left(b_0 - b_{0,3d}\right)}{n_{nef}} \tag{6}$$

b_0 is the length of a basic control perimeter with rounded corners at *d/2* from the column face, v_{c_min} is the shear resistance per unit length given by equation (4) with strain ε_s equal to the reinforcement yield strain ε_{sy} and n_{nef} is total number of joint located within the length depicted V_{1_way} in **Figure 12(b)**.

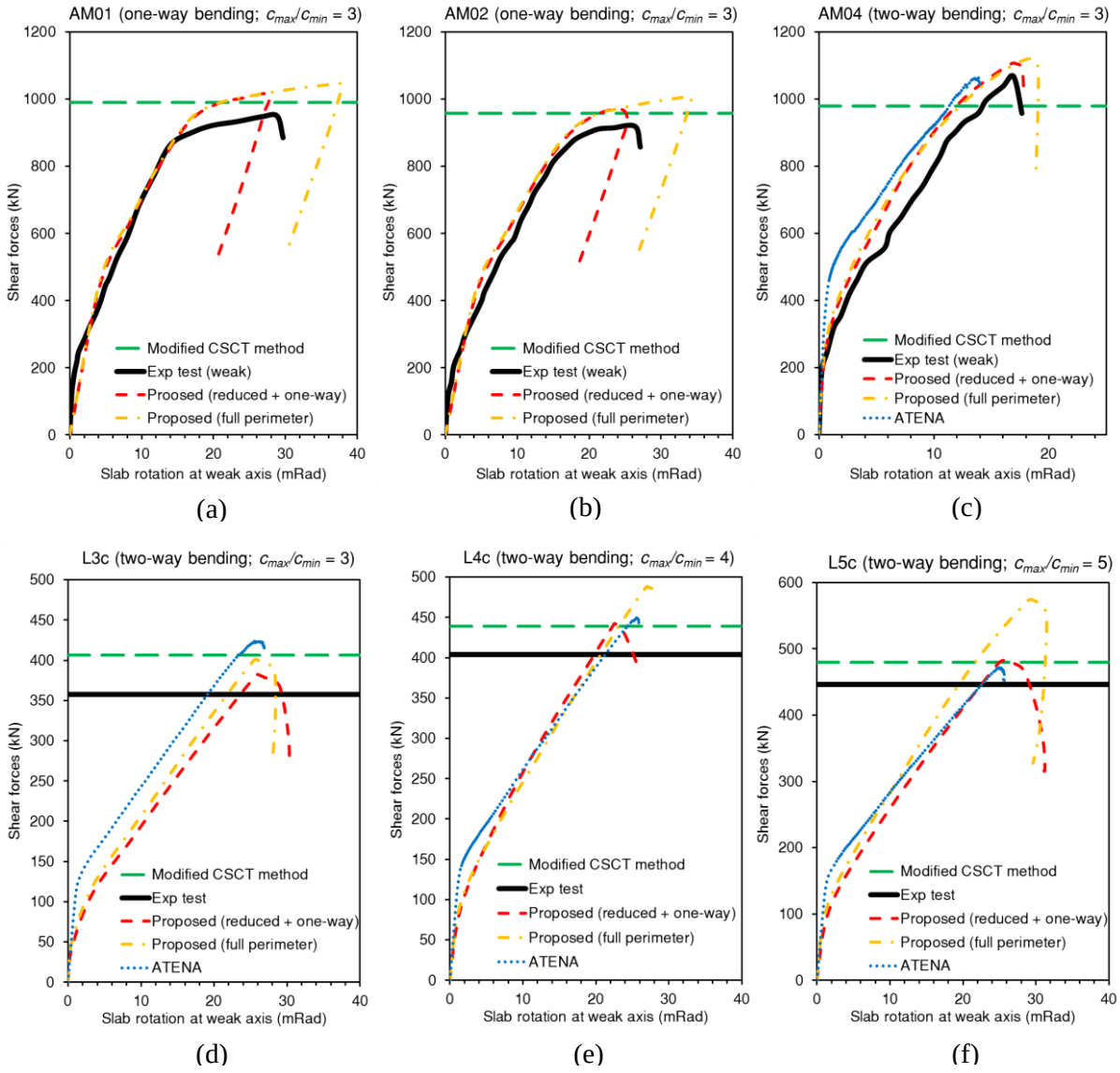

Figure 11. **Load-rotation response and failure point of slabs supported on elongated columns with ratio of longer to shorter side (c_{max}/c_{min}) ranging between 3 and 5: (a) AM01; (b) AM02; (c) AM04 from Sagaseta et al. [39] and (d) L3c; (e) L4c; (f) L5c from Oliveira et al. [40].**

Figure 11 compares the resulting load-rotation responses for the weak-axis of selected slabs with experimental data, where available, or otherwise 3-D NLFEA with ATENA. Measured failure loads are shown along with the predictions of Sagaseta et al. [13] obtained using the $V_{CSCT(\psi x\text{-}\psi y)}$ method (depicted "modified CSCT method"). The latter method accounts for the increase in shear resistance arising from shear redistribution along the effective control perimeter of MC2010 shown in **Figure 12(a)**. All three methods give excellent strength predictions as shown in **Figure 11**. However, the proposed method has the advantage of being much more computationally efficient than 3D analysis with ATENA. Beneficially, the proposed joint model requires no post-processing to determine the intersection of load-rotation and resistance-rotation curves as done in the CSCT [9] and $V_{CSCT(\psi x\text{-}\psi y)}$

[13]. This makes the proposed method suitable for the global analysis of punching shear failure in slabs with multiple columns.

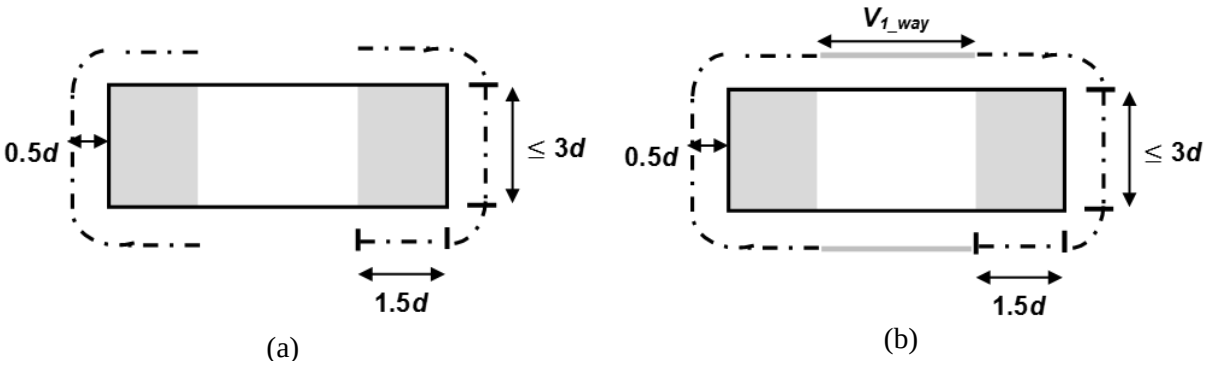

Figure 12. Estimation of effective control perimeter length for slabs supported on rectangular column: a) MC2010; b) proposed.

3.5 Category 3: Eccentric loading

Assessment with the CSCT is complex for eccentric loading since both the slab rotation and shear stress distribution vary non-uniformly around the control perimeter. Recently, Drakatos et al. [42] have proposed an analytical method for finding the moment-rotation response and failure point of eccentrically loaded slabs. The procedure involves integrating shear forces, and shear resistances calculated in terms of slab sector rotations, around the control perimeter. Under monotonic loading failure is assumed to occur when the total shear force acting on the sector elements in the hogging half of the slab equals their resultant shear resistance. This assumption was implemented in the proposed joint model by installing an additional joint element at the junction between the slab and column as shown in **Figure 13.** This "central" joint is needed to limit unbalanced moment transfer to the column. The central joint is coupled with the punching joint located on the axis of the applied unbalanced moment (see **Figure 13**). Failure of the central joint, and hence global connection failure, is triggered by initial failure of the monitored joint element on the axis of applied unbalanced moment.

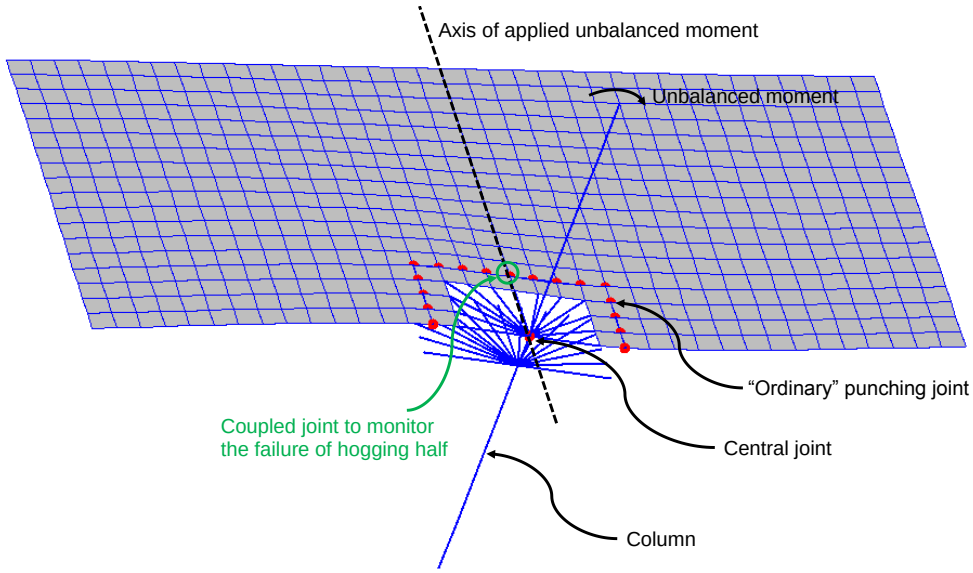

Figure 13. Illustration of additional central joint to trigger punching failure under eccentric load cases.

3.5.1 3a) Constant eccentricity with increasing shear force

This scenario arises under gravity loading in non-symmetric bays of flat slab buildings and can be simulated in the laboratory by applying vertical load at a fixed eccentricity. In total, 11 slabs tested by Hawkins et al. [33] were modelled. The eccentricity was either 130 mm (L) or 577 mm (H). The slabs were grouped into three series as described below:

1) Series A with practical slab dimension (thickness = 153 mm): 4 slabs
2) Series B with thinner slab dimension (thickness = 114 mm): 4 slabs
3) Series C with higher concrete strength (around 60 MPa): 3 slabs

All the slabs measured 2100 mm square on plan and were centrally supported by a 305 mm square column. Unequal vertical forces were applied at 610 mm intervals around the perimeter of the slab to introduce an unbalanced moment at the slab-column connection. The lower end of column was horizontally restrained and a jacking force was applied to the top end of the column to counter balance the uneven load on the slab. Only punching resistance is assessed here since the experimental relative slab column rotation is unknown. **Figure 14** compares the measured slab strengths with the predictions of the proposed methodology, Drakatos et al. [42] and solid element modelling with ATENA. Also shown in **Figure 14** is the sensitivity of the predicted failure load to the joint stiffness reduction factor k_{red}. **Table 3** shows that the adopted value of k_{red} = 0.1 gives good predictions of the measured failure load for a wide range of specimens with both fixed and varying eccentricity.

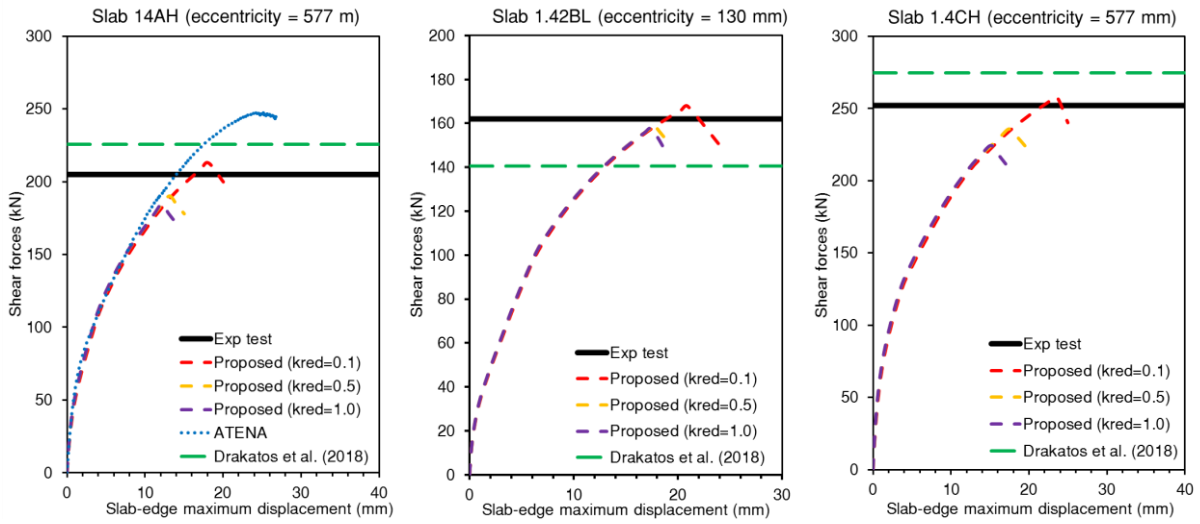

(a) (b) (c)

Figure 13. Load versus slab edge deflection response and failure point of selected slabs of Hawkins et al. [33] in: (a) Series A with *e* = 577 mm; (b) Series B with *e* = 130 mm; and (c) Series C with *e* = 577 mm.

Fig. 14 shows that the model of Drakatos et al. [42] is reasonably accurate. However, the proposed joint model gives better strength predictions due to its more accurate assessment of the proportion of unbalanced moment carried through eccentric shear. Only slab 14AH was modelled using ATENA. The predicted failure load obtained with the proposed approach and ATENA are similar but the former is closer to the experimental result.

3.5.2 3b) Increasing eccentricity with constant shear force

In this series, slabs were loaded with constant shear force at increasing eccentricity until punching failure occurred. The verification considered five monotonically loaded specimens (PD3; PD4; PD5; PD10; PD12) tested by Drakatos et al. [34]. Tested variables were the gravity shear ratio (GSR) and the top flexural reinforcement ratio (ρ_{top}). In this assessment, GSR is defined as the ratio of applied gravity force to the measured punching capacity of a reference slab tested under concentric loading. The slabs of Drakatos et al. measured 3000 mm × 3000 mm × 250 mm and were centrally supported on a 390 mm square steel plate which was clamped to prevent rotation. The gravity load was applied first, followed by increasing unbalanced moment up to failure. **Figure 15** shows the test setup, mesh configuration, and boundary conditions adopted in the NLFEA modelling using ATENA as well as ADAPTIC. The distance between the equal and opposite vertical forces applied to the steel arms represents the slab span between column centrelines as well as the distance between points of contraflexure in adjacent spans under lateral loading.

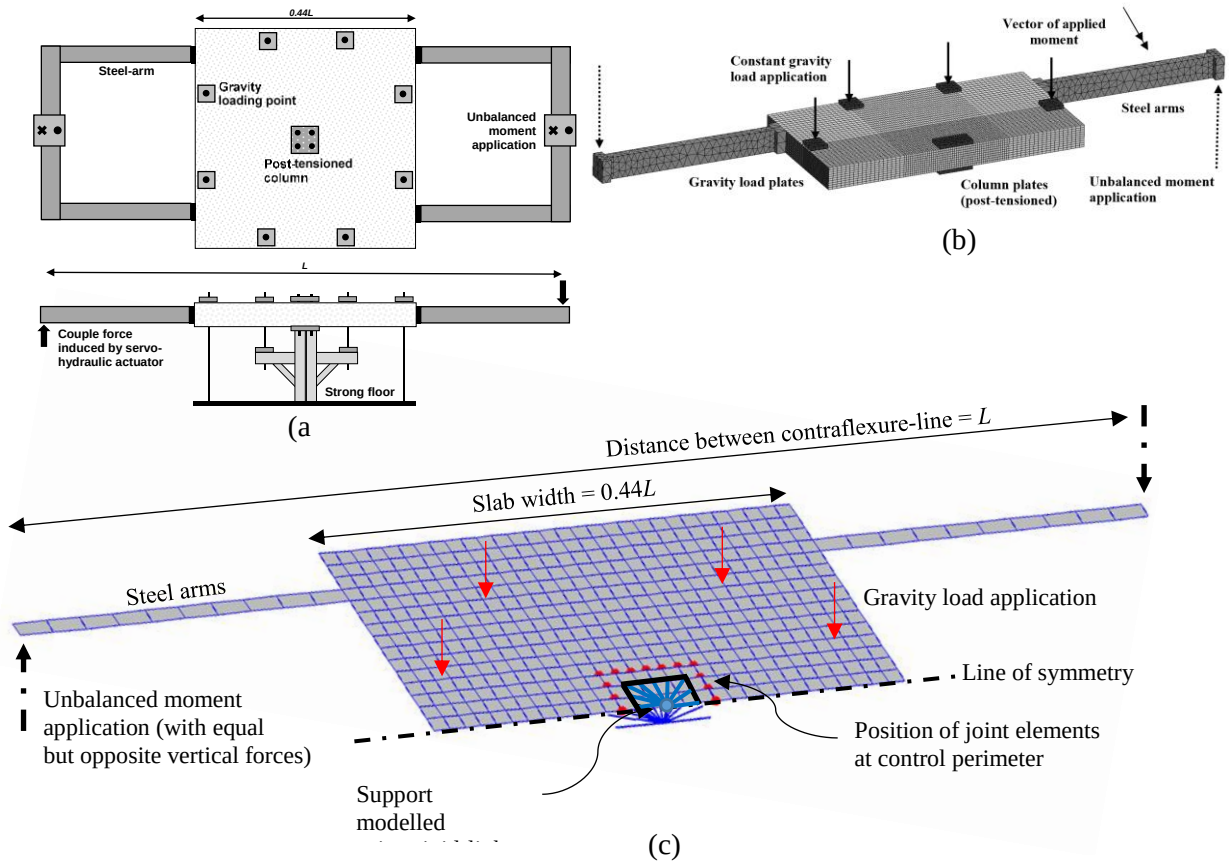

Figure 15. **(a) Test setup and boundary conditions; (b) 3-D solid model in ATENA; (c) Proposed model in ADAPTIC.**

Figure 16 shows experimental and predicted moment-rotation responses for selected slabs. The accuracy of the joint model is seen to be comparable with that obtained using the analytical model of Drakatos et al. [42] and ATENA. **Figure 17** compares deformed shapes obtained with the joint model and ATENA for specimen PD4. In the propoed model, failure of the joints in the hogging half of the slab eventually leads to complete collapse through loss of unbalanced moment carrying capacity in the central joint (see **Figure 13**). The observed crack pattern is also shown for comparison with the 3-D solid element results. **Figure 17** shows that separation of joint elements in the the hogging half of the shell model (around the control perimeter) corresponds to the formation of diagonal cracks in the 3-D solid element model.

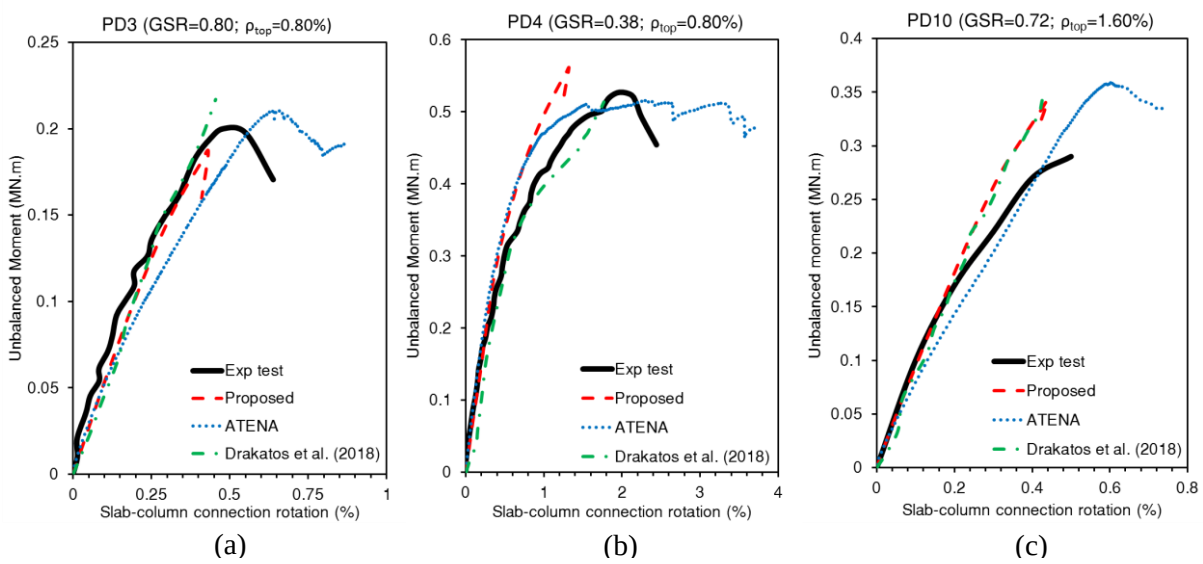

Figure 16. **Moment versus slab-column connection rotation and failure point of slabs with: (a) GSR = 0.80 and ρ_{top} = 0.80%; (b) GSR = 0.38 and ρ_{top} = 0.80%; and (c) GSR = 0.72 and ρ_{top} = 1.60%.**

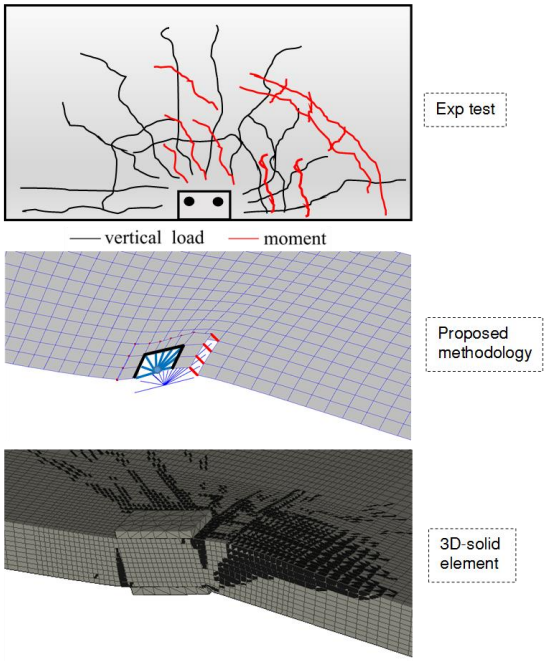

Figure 17. **Deformed shape and crack pattern at failure of specimen PD4 (crack pattern from experimental test is adapted from Drakatos et al., 2016).**

3.6 Discussion

Table 3 shows ratios of measured to predicted punching resistance (P_{test}/P_u) for all the slabs considered in **Sections 3.3** to **3.5**. Results are given for the proposed joint model, the CSCT implemented as described in the footnotes to the table and ATENA where available. The mean value of P_{test}/P_u is very close to 1.0 for both methods which also have similar coefficients of variation of around 10%. **Table 3** confirms that all three of the proposed joint model, the CSCT and ATENA

accurately capture the failure load of isolated slab-column connections subjected to a wide range of loading and boundary conditions.

Table 3. Summary of predictions of the proposed methodology, ATENA and CSCT (original or refined) method

No	Category-series	Series identity	Slab	Source	Measured / Predicted Punching Resistance		
					Refined CSCT method	Proposed methodology	ATENA
1	1a	Flexural reinforcement ratio	PG-5	Guandalini et al. [32]	1.209	1.138	0.953
2			PT22	Sagaseta et al. [13]	1.250	1.059	0.934
3			PT31		1.250	1.112	0.990
4			PG19	Clement et al. [38]	1.170	0.988	-
5			PG20		1.050	1.002	-
6	1b	Size effect	PG-6	Guandalini et al. [32]	1.030	0.943	-
7			PG-7		1.223	1.089	0.910
8			PG-1		1.216	1.113	-
9			PG-11		1.119	0.926	1.008
10			PG-3		1.245	1.027	-
11	1c	In-plane compressive forces	PC5	Clement et al. [38]	1.010	1.243	-
12			PC6		1.060	1.040	-
13			PC7		1.180	1.199	-
14			PC8		1.060	1.086	-
15			PC9		1.110	1.184	-
16			PC10		1.060	1.124	-
17	1d	Post-punching	PM3	Fernandez Ruiz et al. [21]	1.060	1.060	-
18			PM4		1.029	1.029	-
19			PM9		0.909	0.909	-
20			PM10		0.932	0.932	-
21	2a	Non-symmetric reinforcement or loading	PT21	Sagaseta et al. [13]	0.960	0.924	-
22			PT23		0.970	0.889	-
23			PT32		1.200	1.168	1.152
24			PT33		0.932	0.952	0.957
25			PT34		1.000	0.944	-
26	2b	Elongated column	AM01	Sagaseta et al. [13]	0.960	0.935	-
27			AM02		0.960	0.947	-
28			AM04		1.090	0.964	-
29			L3c	Oliveira et al. [40]	0.880	0.935	0.875
30			L4c		0.920	0.913	0.934
31			L5c		0.930	0.923	0.957
32	3a	Monotonic constant eccentricity	9.6AH	Hawkins et al. [33]	0.969	0.995	-
33			14AH		0.908	0.963	0.830
34			9.6AL		0.911	0.883	-
35			14AL		0.998	0.991	-

36			9.5BH		0.918	0.975	-
37			14.2BH		0.912	0.959	-
38			9.5BL		0.985	0.889	-
39			14.2BL		1.152	0.966	-
40			9.6CH		0.864	0.988	-
41			14CH		0.918	0.978	-
42			14CL		0.965	0.962	-
43	3b	Monotonic increasing eccentricity	PD4	Drakatos et al. [34]	1.026	0.939	0.985
44			PD5		0.979	1.161	0.919
45			PD3		0.938	1.070	0.975
46			PD12		0.914	0.815	0.872
47			PD10		0.855	0.847	1.004
				Mean	**1.025**	**1.002**	**0.953**
				Standard deviation	**0.114**	**0.097**	**0.071**
				CoV (%)	**11.07%**	**9.69%**	**7.40%**

Notes:

† indicates refined CSCT method considering the reduction of cracked effective depth due to the presence of compressive membrane forces proposed by [38]
*** presents the measured to predicted post-punching resistance calculated based on the mechanical model of [21]**
§ indicates refined CSCT method considering shear redistribution of non-axis-symmetric slabs proposed by [13]
• indicates refined CSCT method for the case of slabs subject to eccentric loading condition proposed by [42]

4 Discussion of local joint response

Besides excellent accuracy, the proposed methodology allows investigation of joint forces along the control perimeter. This provides enhanced understanding of load transfer between the slab and column which is pertinent to the development of improved codified design methods.

4.1 Shear forces variation along the control perimeter

The verification analyses show that the proposed methodology models shear redistribution of the type identified by Sagaseta et al. [13] in which failure of the first joint element leads to shear force being redistributed to adjacent joint elements under increasing load. **Figure 18** shows joint shear forces at four different loads for specimen PT34, which was subject to one-way bending. Forces are shown in **Figure 18(a)** and **Figure 18(b)** respectively for joints positioned along control perimeter sides perpendicular and parallel to the bending axis. Joint positions are shown in **Figure 18(c)**. Shear forces in joints oriented along the bending-axis (see **Figure 18(b)**) only increased slightly between $0.75P_u$

and $0.95P_u$ (where P_u is the calculated failure load). Subsequently, the forces in these joints softened as the load was increased from $0.95P_u$ to failure. This softening was accompanied by an increase in joint shear forces along the non-bending-axis in the three joints closest to the slab centreline (with ordinates of 0 mm; 50 mm; and 100 mm) (see **Figure 18(a)**). Global connection failure occurred when these three joints failed almost simultaneously at the joint shear forces depicted by asterisks in **Figure 18(a)**.

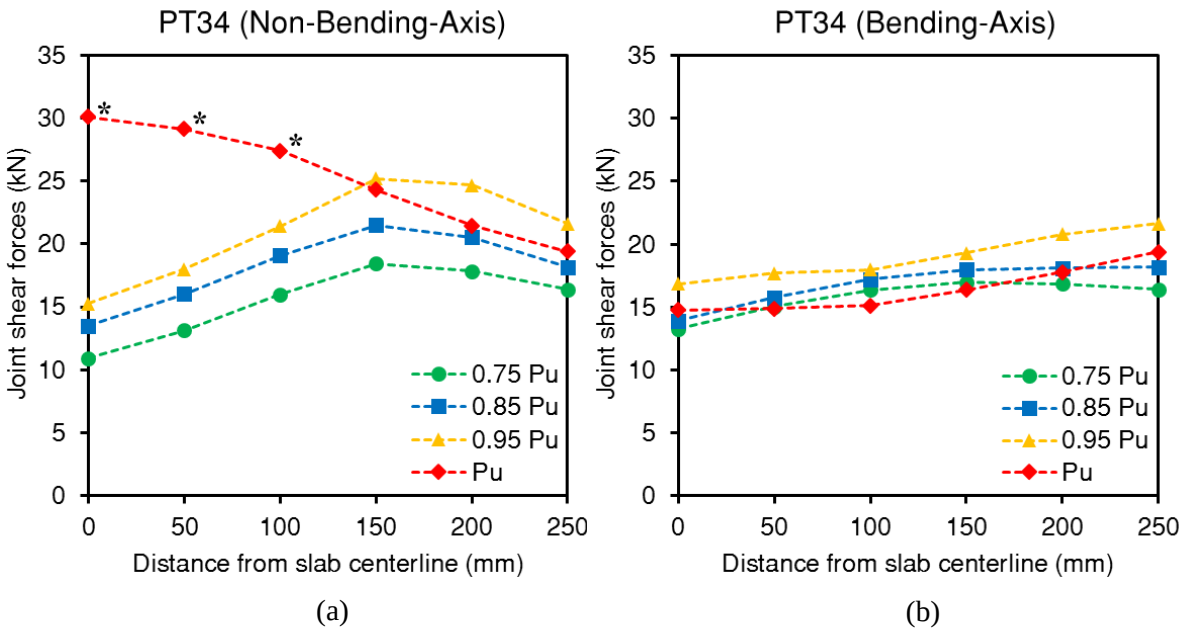

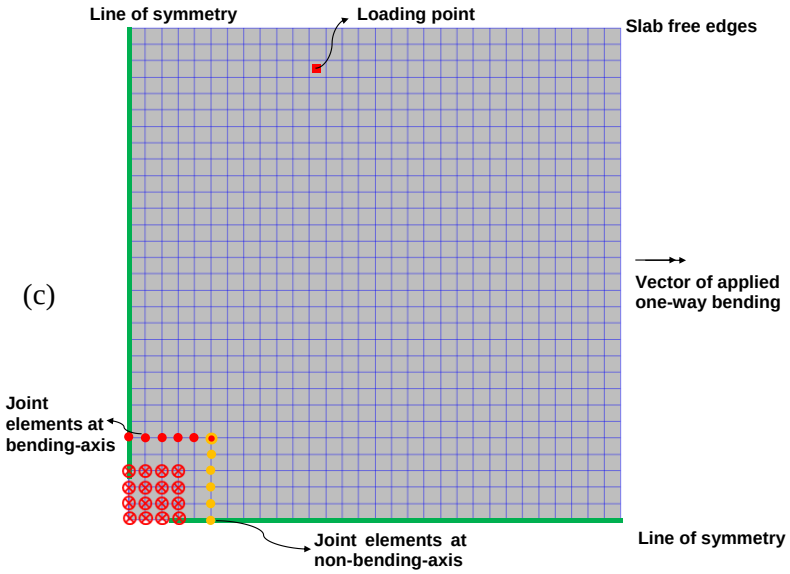

Figure 18. **Prediction of local joint forces along: (a) non-bending axis; (b) bending axis of specimen PT34 and (c) slab plan view showing the position of joint elements along the control perimeter.**
(Notes: positive sign indicates downward shear force)

4.2 Joint properties for slabs supported on elongated-columns

As shown in **Figure 12(a)**, MC2010 limits the total straight length of the control perimeter on each side of the column to a maximum of 3*d*. In the proposed joint model, the shear resistance of the straight lengths discounted by MC2010 are modelled using joint elements having the nominal one-way shear resistance defined in **Section 3.4.2**. **Figure 19** illustrates the effect of introducing one-way shear joints on the variation in joint shear force around the control perimeter for specimen L5c with c_{max}/c_{min} of 5. The joint location is shown in **Figure 19(a)** while **Figure 19(b)** shows joint shear forces at four different load stages. At $0.75P_u$, the joint shear force distribution is almost uniform along the shorter side of the control perimeter with joint shear force equal to the peak resistance. Between $0.75P_u$ and failure, the joint shear forces on the short side decrease by around 20% due to softening. The shear force distribution is much less even along the long side of the control perimeter (see **Figure 19(c)**) with negative (upward) forces occurring in joints with one-way shear resistance between $0.50P_u$ and $0.75\ P_u$. Force is transferred to the long sides of the control perimeter as the joints soften on the short side. Global shear failure was triggered by failure of the joint positioned at the centre of the long column side.

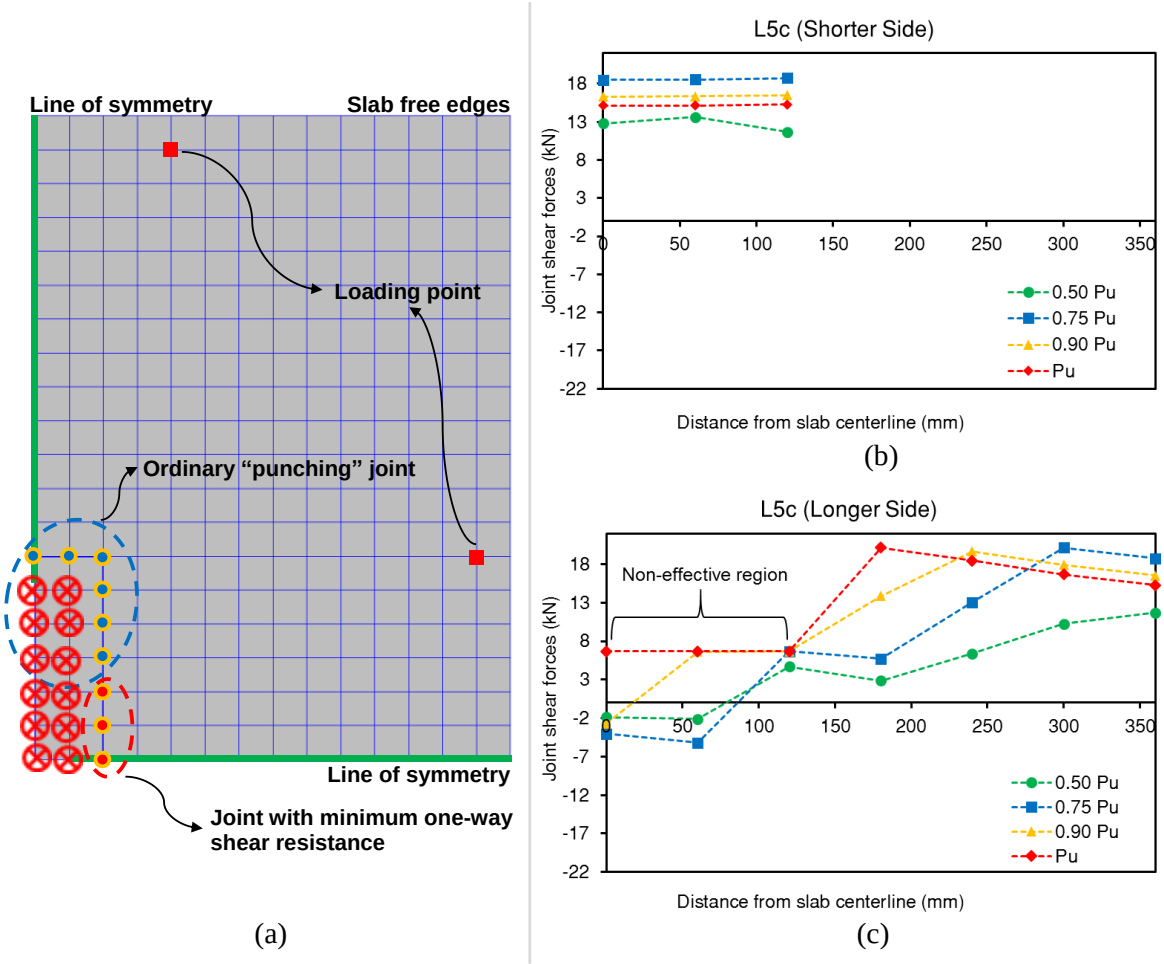

Figure 19. **(a) Implementation of joint element with minimum one-way shear resistance and variation of joint local forces at: (b) shorter and (c) longer side of the control perimeter of specimen L5c.**
(Notes: positive sign indicates downward shear force)

4.3 Contribution of individual lateral load resisting mechanisms

For slabs subject to increasing eccentricity, unbalanced moment due to lateral loading is resisted by flexure, eccentric shear, and torsion. In design, it is necessary to account for the increase in shear stress due to moment transfer. For example, in the case of square columns, ACI 318-14 [1] assumes that 40% of the unbalanced moment is resisted by eccentric shear. In reality, the internal force distribution is more complex and still the subject of research [17, 20, 26, 42]. The proposed joint model is a convenient tool for studying this problem. By extracting internal forces from each joint element, the contribution of each lateral resisting mechanism can be quantified in terms of slab-column connection rotation as shown in **Figure 20** for specimens PD4 and PD10 of Drakatos et al. [34].

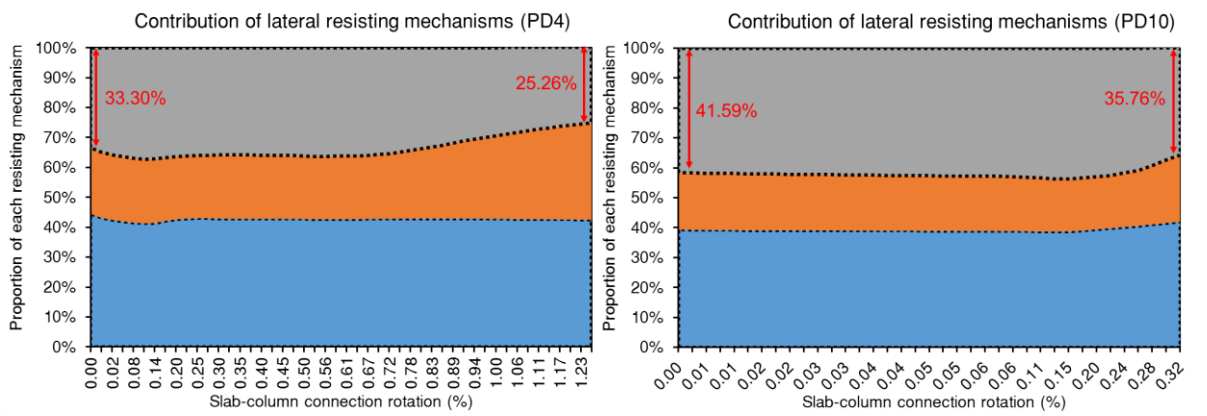

(a) (b)

Figure 20. Contribution of each resisting mechanism as a function of slab-column connection rotation of slab: (a) PD4 and (b) PD10 till the peak unbalanced moment.
Notes: slab-column connection rotation reported in x-axis is not scaled linearly

Figure 20 shows that the proportion of unbalanced moment carried by eccentric shear is initially around 30 – 40% for both specimens which is comparable to the estimation of ACI 318-14 [1]. For both specimens, the contribution of eccentric shear to unbalanced moment reduces when failure of the joints on the hogging side causes shear to be redistributed to the side faces. The reduction in the eccentric shear contribution is offset by a simultaneous increase in the torsional (side-face) contribution. At punching failure, the proportion of unbalanced moment resisted by eccentric shear is 5-10% less than initially.

5 Conclusion

This paper presents a novel numerical methodology for modelling punching shear failure in flat slabs using joint elements connected to shell elements. The procedure is implemented in the finite element code ADAPTIC [22]. Joint elements are distributed uniformly along a rectangular control perimeter located at 0.5*d* from the column face and connect the shell elements inside and outside of the control perimeter. In order to detect the occurrence of punching, the CSCT failure criterion [9] is implemented within the formulation of the joint element. Each joint is associated with a radial sector of the slab. The joint shear resistance is calculated at each load step in terms of its sector rotation relative to the column. This allows joint failure to be detected without the need to pre-determine joint shear capacity as done in previous studies [8, 11, 12]. In the proposed model, failure of the first joint element does not generally trigger global failure since additional load is subsequently transferred to other joint elements, hence simulating shear redistribution.

In order to verify the proposed methodology, a total of 47 punching tests from the literature were analysed. The tests were grouped into three main test categories namely: 1) axis-symmetric; 2) non-axis-symmetric; and 3) eccentric. Analysis shows that the proposed methodology is capable of

accurately capturing both the load-rotation response and the failure point. Shear redistribution, which increases the calculated punching capacity of slabs in categories 2) and 3), was reproduced appropriately. Results obtained using the joint model predictions are comparable to those obtained using the refined CSCT method of Sagaseta et al. [13] demonstrating that the joint model works as intended. The accuracy of the proposed joint model is also comparable with the presented 3-D solid element modelling with ATENA which is much more computationally intensive. The computational efficiency of the proposed methodology makes it suitable for the assessment of global building behaviour. Furthermore, analysis of joint shear forces also provides novel insights into shear redistribution and lateral load resisting mechanisms at a local perspective.

Acknowledgement

The work presented in this article was supported by the Indonesia Endowment Fund for Education (LPDP). The opinions and conclusions in this document are those of the authors, and do not necessarily represent those of the sponsors.

References

[1] ACI Committee 318, 2014. ACI Building Code Requirements for Structural Concrete (ACI 318-14) and Commentary (ACI 318R-14). American Concrete Institute, Farmington Hills, MI, 519 pp.

[2] BSI, 2004. BS EN 1992-1-1:2004: Eurocode 2, design of concrete structures – part 1-1: general rules and rules for buildings. BSI, London, UK.

[3] Einpaul, J., Ospina, C. E., Ruiz, M. F. & Muttoni, A., 2016. *Punching shear capacity of continuous slabs*. *ACI Structural Journal*, 113(4), pp.861–872.

[4] Polak, M. A., 2005. *Shell finite element analysis of RC plates supported on columns for punching shear and flexure*. *Engineering Computations*, 22(4), pp.409–428.

[5] Vecchio, F. J., and Collins, M. P., 1986. *The modified compression-field theory for reinforced concrete elements subjected to shear*. *ACI Structural Journal*, 83(2), 219–231.

[6] Hrynyk, T. D. and Vecchio, F. J., 2015. *Capturing Out-of-Plane Shear Failures in the Analysis of Reinforced Concrete Shells*. *Journal of Structural Engineering*, 141(12): 04015058.

[7] Vecchio, F. J., 2000. *Disturbed stress field model for reinforced concrete: Formulation. Journal of Structural Engineering*, 10.1061/(ASCE)0733-9445(2000)126: 9(1070), 1070–1077.

[8] Keyvani, L., Sasani, M. & Mirzaei, Y., 2014. *Compressive membrane action in progressive collapse resistance of RC flat plates*. *Engineering Structures*, 59, pp.554–564.

[9] Muttoni, A., 2008. *Punching Shear Strength of Reinforced Concrete Slabs without Transverse Reinforcement*, *ACI Structural Journal*, V. 105, No. 4, pp. 440-450.

[10] Mirzaei, Y. Post-punching behavior of Reinforced concrete slabs. PhD thesis, École Polytechnique Fédérale de Lausanne, Switzerland; 2010. 230p.

[11] Liu, J., Tian, Y., Orton, S. L. & Said, A. M., 2015. *Resistance of Flat-Plate Buildings against Progressive Collapse*. *Part I : Modeling of Slab-Column Connections*. *Journal of Structural Engineering*, 141(12).

[12] Liu, J., Tian, Y., Orton, S. L. & Said, A. M., 2015. *Resistance of Flat-Plate Buildings against Progressive Collapse*. *Part II : System Response*. *Journal of Structural Engineering*, 141(12).

[13] Sagaseta, J., Muttoni, A., Ruiz, M. F. & Tassinari, L., 2011. *Non-axis-symmetrical punching shear around internal columns of RC slabs without transverse reinforcement*. *Magazine of Concrete Research*, 63(6), pp.441–457.

[14] Yamazaki, J. and Hawkins, N. M., 1980. *Finite Element Predictions of the Behavior of Slab-Column Connections Transferring Moment*. *ACI Structural Journal*, Special Publication 63.
[15] Genikomsou, A. S. and Polak, M. A., 2015. *Finite element analysis of punching shear of concrete slabs using damaged plasticity model in ABAQUS*. *Engineering Structures*, 98, pp.38–48.
[16] Hillerborg, A., Modeer, M. & Petterson, P.E., 1976. *Analysis of crack formation and crack growth in concrete by means of fracture mechanics and finite elements*. *Cement Concrete Res*; 6:773-82.
[17] Shu, J., Belletti, B., Muttoni, A., Scolari, M. & Plos, M., 2017. *Internal force distribution in RC slabs subjected to punching shear*. *Engineering Structures*, 153, pp.766–781.
[18] Vollum R.L., Abdel Fattah T., Eder M. and Elghazouli A.Y., "Design of ACI type punching shear reinforcement to Eurocode 2", Magazine of Concrete Research, 62, (2010), 3-16.
[19] Eder M.A, Vollum R.L., Elghazouli A.Y., Abdel-Fattah T., "Modelling and experimental assessment of punching shear in flat slabs with shearheads", Engineering Structures, 32 (2010), pp. 3911-3924.
[20] Soares, L. F. S. and Vollum, R. L., 2016. *Influence of continuity on punching resistance at edge columns*. *Magazine of Concrete Research*, 68(23): 1225-1239.
[21] Fernández Ruiz, M., Mirzaei, Y. & Muttoni, A., 2013. *Post-punching behavior of flat slabs*. *ACI Structural Journal*, 110(5), pp.801–811.
[22] Izzuddin, B. A., *Nonlinear Dynamic Analysis of Framed Structures*, Thesis submitted for the degree of doctor of philosophy in the University of London, Department of Civil Engineering, Imperial College, London, 1991.
[23] Izzuddin, B.A., Tao, X.Y. & Elghazouli, A.Y., 2004. *Realistic Modeling of Composite and Reinforced Concrete Floor Slabs under Extreme Loading*. *Part I: Analytical Method*. *Journal of Structural Engineering*, 130(12), pp.1972–1984.
[24] Izzuddin BA, Liang Y, Bisector and zero-macrospin co-rotational systems for shell elements, Int J Numer Meth Engng 2016; 105:286–320
[25] Izzuddin, B.A., 2016, ADAPTIC User Manual, Imperial College London, https://www.imperial.ac.uk/media/imperial-college/research-centres-and-groups/computational-structural-mechanics/ADAPTIC_Manual.pdf
[26] Broms, C. E., 2016. *Tangential Strain Theory for Punching Failure of Flat Slabs*, *ACI Structural Journal*, V. 113, No. 1, pp. 95-104.
[27] Cervenka, V., Jendele, L. & Cervenka, J., 2007. *ATENA Program Documentation, Part 1, Theory*. Cervenka Consulting, Prague, 231.
[28] Menetrey, P. and Willam, K.J., 1995. *Triaxial failure criterion for concrete and its generalization*. *ACI Structural Journal*, 92(3), pp.311–318.
[29] Van Mier J. G. M., 1986. *Multi-axial Strain-softening of Concrete, Part I: fracture, Materials and Structures*, RILEM, 19(111).
[30] CEB-FIP MC90, 1993, *Design of Concrete Structures-CEB-FIP-Model Code 1990*, Thomas Telford, London, UK, 437 pp.
[31] fib (Fédération International du Béton), 2013. fib Model Code for concrete structures 2010. Fédération International du Béton, Lausanne, Switzerland.
[32] Guandalini, S., Burdet, O. L. & Muttoni, A., 2009. *Punching tests of slabs with low reinforcement ratios*. *ACI Structural Journal*, 106(1), pp.87–95.
[33] Hawkins, N. M., Bao, A. & Yamazaki, J., 1989. *Moment Transfer from Concrete Slabs to Columns*. *ACI Structural Journal* 86(6).
[34] Drakatos, I.S., Muttoni, A. & Beyer, K., 2016. *Internal slab-column connections under monotonic and cyclic imposed rotations*. *Engineering Structures*, 123, pp.501–516.
[35] Elghazouli, A.Y, Izzuddin, B.A., 2004. *Realistic Modeling of Composite and Reinforced Concrete Floor Slabs under Extreme Loading. II: Verification and Application*. *Journal of Structural Engineering*, 130(12), pp.1985–1996.
[36] Rots JG. *Computational modelling of concrete fracture*. Doctoral thesis, Technical University of Delft; 1988. p. 132
[37] Vollum, R.L. and Tay U.L., "Modelling tension stiffening in reinforced concrete with NLFEA", Concrete, 41, 1, (2007), 40-41.
[38] Clément, T., Ramos, A. P., Ruiz, M. F. & Muttoni, A., 2014. *Influence of prestressing on the punching strength of post-tensioned slabs*. *Engineering Structures*, 72, pp.56–69.

[39] Sagaseta, J., Tassinari, L., Ruiz, M. F. & Muttoni, A., 2014. *Punching of flat slabs supported on rectangular columns*. *Engineering Structures*, 77, pp.17–33.
[40] Oliveira, D. R. C., Regan, P. E. & Melo, G. S. S. A., 2004. *Punching resistance of RC slabs with rectangular columns*. *Magazine of Concrete Research*, (3), pp.123–138.
[41] Cavagnis, F., Ruiz, M.F. & Muttoni, A., 2018. *A mechanical model for failures in shear of members without transverse reinforcement based on development of a critical shear crack*. *Engineering Structures*, 157, pp.300–315.
[42] Drakatos, I.S., Muttoni, A. & Beyer, K., 2018. *Mechanical Model for Drift-Induced Punching of Slab-Column Connections without Transverse Reinforcement*. *ACI Structural Journal*, 115(2).